AMERICAN METEOROLOGICAL SOCIETY

Journal of Climate

EARLY ONLINE RELEASE

The DOI for this manuscript is doi: 10.1175/JCLI-D-17-0172.1

The final published version of this manuscript will replace the preliminary version at the above DOI once it is available.

If you would like to cite this EOR in a separate work, please use the following full citation:

Cook, B., A. Williams, J. Mankin, R. Seager, J. Smerdon, and D. Singh, 2017: Revisiting the leading drivers of Pacific coastal drought variability in the Contiguous United States. J. Climate. doi:10.1175/JCLI-D-17-0172.1, in press.

Revisiting the leading drivers of Pacific coastal drought variability in the Contiguous United States

Benjamin I. Cook*

NASA Goddard Institute for Space Studies, New York, New York; Division of Ocean and Climate Physics, Lamont-Doherty Earth Observatory, Palisades, New York, USA

A. Park Williams

Tree Ring Lab, Lamont-Doherty Earth Observatory, Palisades, New York, USA

Justin S. Mankin

NASA Goddard Institute for Space Studies; Division of Ocean and Climate Physics, Lamont-Doherty Earth Observatory, Palisades, New York, USA

Richard Seager, Jason E. Smerdon, Deepti Singh

Division of Ocean and Climate Physics, Lamont-Doherty Earth Observatory, Palisades, New York, USA

* *Corresponding author address:* Benjamin I Cook, NASA Goddard Institute for Space Studies, 2880 Broadway, New York, NY 10025.

E-mail: benjamin.i.cook@nasa.gov

ABSTRACT

Coastal droughts simultaneously affecting California, Oregon, and Washington are rare, but have extensive and severe impacts (e.g., wildfire, agriculture). To better understand these events, we use historical observations to investigate: (1) drought variability along the Pacific Coast of the Contiguous United States and (2) years when extreme drought affects the entire coast. The leading pattern of cold-season (October–March) precipitation variability along the Pacific Coast favors spatially coherent moisture anomalies, accounts for $> 40\%$ of the underlying variance, and is forced primarily by internal atmospheric dynamics. This contrasts with a much weaker dipole mode ($\sim 20\%$ of precipitation variability) characterized by anti-phased moisture anomalies across 40^{o}N and strong correlations with tropical Pacific sea surface temperatures (SSTs). Sixteen coastal-wide summer droughts occurred from 1895–2016 (clustering in the 1920s–1930s and post-2000), events most strongly linked with the leading precipitation mode and internal atmospheric variability. The frequency of landfalling atmospheric rivers south of 40^{o}N is sharply reduced during coastal droughts, but not north of this boundary where their frequency is more strongly influenced by the dipole. The lack of a consistent pattern of SST forcing during coastal droughts suggests little potential for skillful seasonal predictions. However, their tendency to cluster in time and the impact of warming during recent droughts may help inform decadal and longer-term drought risks.

1. Introduction

In 2015, moderate to exceptional drought covered nearly all of the Contiguous United States (CONUS) from Colorado to the Pacific Coast (Fuchs 2015). This included the continuation of multi-year events in California (Griffin and Anchukaitis 2014; Seager et al. 2015; Williams et al. 2015) and the Southwest (Delworth et al. 2015; Seager and Hoerling 2014) and the emergence of significant drought conditions across the Pacific Northwest (Oregon, Washington) (Mote et al. 2016). Drought anomalies were especially severe in the three Pacific coastal states.

For California, 2015 ranked as the single worst year of drought on record in terms of April 1 snow water equivalent and August–July unimpaired natural runoff (He et al. 2017). In the Pacific Northwest, record warmth drove record low snowpack across Oregon and Washington (Mote et al. 2016). By spring of 2015, drought emergencies were declared in all three of the Pacific CONUS states (Lurie 2015; Wise 2016), conditions that contributed to the worst wildfire year in the United States since modern record keeping began in 1960 (Dickie 2016). Seven of the ten largest wildfires that year occurred in California and the Pacific Northwest, over 10 million total acres burned across the CONUS and Alaska, and 52% of the annual US Forest Service budget was spent on wildfire related expenses (Dickie 2016; Kahn 2016; Roman 2015). The 2015 drought also caused significant agricultural and economic losses, costing California $2.7 billion and 21,000 jobs (Daniels 2016; Rice 2015) and Washington state over $700 million (Jenkins 2017).

Extensive coastal droughts that simultaneously affect California and the Pacific Northwest, as occurred in 2015, have often been considered rare relative to other drought patterns. Wise (2016), for example, observed that west-coast wide drought events occur less frequently than more regional drought patterns characterized by out-of-phase moisture anomalies in the meridional direction (e.g., a simultaneously wet Pacific Northwest and dry California). This is likely due, in part,

to the impact of two of the most important climate teleconnections in the western CONUS: the El Niño Southern Oscillation (ENSO) and the Pacific Decadal Oscillation (PDO). These modes favor out-of-phase precipitation and drought anomalies in the meriodional direction that would oppose the development of co-occurring dry (or wet) conditions along the entire CONUS Pacific Coast. During cold phases (La Niña and negative PDO), the winter storm tracks that supply most of the moisture to the west are shifted northward, favoring increased precipitation in the Pacific Northwest and reduced precipitation in the Southwest and southern US (Dettinger et al. 1998; McCabe et al. 2004; Piechota and Dracup 1996; Redmond and Koch 1991). These patterns are reversed during warm phases (El Niño and positive PDO), when the storm tracks are preferentially shifted southward. These dynamics give rise to a "dipole" pattern of anti-phased hydroclimate variability that has been documented in precipitation (Brown and Comrie 2004; Dettinger et al. 1998; Wise 2010), streamflow (Meko and Stockton 1984), and other drought indicators (Woodhouse et al. 2009). Along the Pacific Coast, the transition latitude between the dipole centers of action, across which moisture anomalies are expected to reverse sign, is 40°N–42°N (e.g., Wise 2010, 2016), separating the Pacific Northwest and northern California from central and southern California.

Recently, however, there has been increased interest in understanding factors influencing hydroclimate variability from dynamics outside of the dipole paradigm. This is because teleconnections between North America and ENSO/PDO dynamics may lack the strength to overwhelm internal atmospheric variability (Cole and Cook 1998; McAfee 2014; McAfee and Wise 2016), especially during certain seasons when ENSO teleconnections are weaker (e.g., fall and early winter) (Diaz et al. 2001; Jong et al. 2016; McAfee and Wise 2016). It is therefore difficult to rely on these modes alone to develop robust hydroclimate predictions. This was illustrated most recently by the failure of the strong 2015–2016 El Niño to bring meaningful drought relief to California and the western CONUS (Kintisch 2016; Wanders et al. 2017).

Further complicating predictions along the Pacific Coast are sub-seasonal dynamics related to atmospheric rivers (AR), narrow corridors of intense horizontal water vapor transport (Gimeno et al. 2014). The precipitation events associated with the relatively few landfalling ARs every year are disproportionally large contributors to total cold season precipitation along the Pacific Coast (Dettinger 2013; Rutz et al. 2013), especially in California. A small increase or decrease in the number of AR events can thus make the difference between plunging a region into a significant drought (Dettinger et al. 2011) or ending an existing drought (Dettinger 2013). There is little consensus, however, on ENSO/PDO impacts on atmospheric rivers (Gimeno et al. 2014). Dettinger et al. (2011), for example, found that significant correlations between ENSO/PDO and AR contributions to precipitation along the Pacific Coast were confined primarily to southern California, while other studies suggest ARs may be stronger or more frequent during neutral ENSO phases (Bao et al. 2006; Dettinger 2004).

Other studies have shown that at the monthly to seasonal scale, the leading mode of hydroclimate variability along the Pacific Coast is not an ENSO-like dipole, but instead a spatially-coherent mode that is in phase across the western CONUS. Such a pattern was documented in the early 1980s for precipitation along the Pacific Coast (Cayan and Roads 1984; McGuirk 1982), and later for streamflow (Cayan and Peterson 1989; Cayan et al. 2003; Malevich and Woodhouse 2017) and spring snowpack (McCabe and Dettinger 2002). This mode is strongly correlated with extratropical atmospheric circulation anomalies in the North Pacific that occur largely independent of tropical ocean forcing. In wet years on the Pacific Coast, low pressure anomalies are centered offshore to the northwest, favoring anomalous cyclonic circulation and southwesterly flow into North America (Klein 1965). During widespread droughts (such as occurred in 2015), persistent atmospheric ridging deflects storms away from the entire coast (Cayan and Roads 1984; Seager et al. 2015; Swain et al. 2014, 2016; Wise 2016).

The relative importance of these various processes and modes of variability will thus have significant consequences for our understanding of drought variability and risk along the CONUS Pacific Coast, especially for the most widespread drought events. Here, we revisit the dominant modes of variability in the region to better clarify their importance for hydroclimate and their contribution to the most widespread coastal droughts. We analyze instrumental records of climate over the recent historical period (1895–2016) to investigate the following questions: 1) How strongly do precipitation and drought covary along the CONUS Pacific Coast?; 2) What is the relative importance of the dipole versus coastal-wide mode for drought variability along the Pacific Coast?; 3) How often do major coastal droughts occur that affect the entire CONUS Pacific Coast?; and 4) What is the relative importance of ocean forcing versus internal atmospheric variability in causing these droughts?

2. Methods and Data

Climate Data

Gridded monthly precipitation totals, mean daily maximum temperatures, and mean daily minimum temperatures were accessed from the ClimGrid dataset produced by the National Oceanic and Atmospheric Administration (Vose et al. 2014). These gridded datasets have 1/24^{o} geographic resolution and cover 1895–2016. ClimGrid temperatures were calibrated to the gridded version 1.2.0 TopoWx temperature dataset (Oyler et al. 2015) such that the two datasets agreed in terms of monthly means and standard deviations during 1961–2010 (e.g., Williams et al. 2015). TopoWx better represents temperature at higher elevations in the western US (Oyler et al. 2015) but does not cover the entire period of study. For drought calculations, atmospheric evaporative demand was represented as the Penman-Monteith reference evapotranspiration (Monteith 1965), which is

a model estimate of evapotranspiration from an idealized crop when water is not limiting. Monthly input variables are temperature, vapor pressure, wind speed, and solar radiation. Vapor pressure was calculated from monthly 1/24^{o} grids of mean dew point from the PRISM group at Oregon State University (Daly et al. 2008). Wind speed was calculated at 2 meters above the surface and net downward solar radiation at the surface, compiled from multiple sources. The National Land Data Assimilation System version 2 (NLDAS2; Mitchell et al. 2004) data were used for 1979–2016 and extended back to 1948 by calibrating data from the Global Land Data Assimilation System (GLDAS; Rodell et al. 2004) to NLDAS2 for the overlapping period of 1979–2010. We refer to the resultant dataset as LDAS. The LDAS records were extended back to 1901 using the Princeton Global Forcing dataset (PGF; available 1901–2014) (Sheffield et al. 2006), calibrated to LDAS during 1961–2010. Because the PGF dataset begins in 1901, we held wind speed and solar radiation to their monthly means for 1895–1900. For vapor pressure, wind speed, and solar radiation, each dataset has a different geographic resolution and all records were bilinearly interpolated to a common resolution of 1/4^{o}. The LDAS dataset represents wind speeds at 10 meters above the surface so we applied a logarithmic wind profile following Allen et al. (1998) to estimate wind speed at 2 meters. Downward solar radiation values were converted to net solar radiation values by applying the mean monthly NLDAS2 albedo climatology for 1979–2010 (our assumption of no interannual variability in albedo was found to have negligible impacts on drought calculations in exploratory analysis). Finally, precipitation and temperature grids were aggregated to a 1/4^{o} geographic resolution for calculations of reference evapotranspiration and drought.

To define summer drought, we use summer season (June-July-August; JJA) average values of the self-calibrating Palmer Drought Severity Index (PDSI; Palmer 1965; Wells et al. 2004) calculated from these instrumental datasets. PDSI is a normalized index of drought (soil moisture), integrating changes in supply (precipitation) and demand (evapotranspiration) over multiple seasons,

therefore making it an appropriate index for analyzing drought even over regions where moisture supply is dominated by cold season precipitation (e.g., the Pacific Coast of North America). Negative (positive) values indicate dry (wet) conditions relative to a baseline average of zero (values of −1 are considered a 'moderate' drought). PDSI is widely used in observational analyses (Trenberth et al. 2014), as a target for tree-ring based paleoclimate reconstructions (Cook et al. 2004), and to investigate drought dynamics in model simulations (Coats et al. 2015; Cook et al. 2014, 2015; Dai 2013; Feng et al. 2017). Drought variability in PDSI compares favorably with soil moisture from more sophisticated land surface models (Cook et al. 2015; Feng et al. 2017), even in regions strongly dominated by snow (a process not explicitly simulated in the PDSI calculations), such as the Sierra Nevada Mountains (e.g., Williams et al. 2015).

The climate datasets and PDSI used here were developed previously for a study investigating climate change contributions to the recent California drought (Williams et al. 2015). As part of that study, these data were compared against alternative datasets, and their variability, trends, and effects on PDSI calculations were also extensively assessed. The ClimGrid temperature and precipitation closely track the variability and trends of data from other sources (e.g., precipitation from the Global Precipitation Climatology Centre, temperature from the Berkeley Earth Surface Temperature project). Calculations of atmospheric moisture demand (potential evapotranspiration) and PDSI across these different temperature and precipitation datasets yielded near identical results across the entire period of record (Figure 1a,c,h in Williams et al. 2015). The largest uncertainties are likely in the estimates of potential evapotranspiration derived from humidity, wind speed, and solar radiation, which differ substantially between datasets, especially prior to 1950 (Figure 1e,f,g in Williams et al. 2015). Despite these differences, Williams et al. (2015) show that humidity, wind speed, and solar radiation are far less important than precipitation and temperature in terms of driving PDSI variability and trends in California, and we find this to be true

throughout our west-coast study region. Importantly, uncertainty may also be introduced through our method of temporally extending the wind speed and solar radiation data, because combining two datasets with differing spatial resolutions, even if calibrated temporally, may still influence temporal variability in regionally-averaged timeseries. The minimal contribution of wind speed and solar radiation to inter-annual PDSI variability in our study region dictates that any artificial shifts in temporal variability in wind speed or solar radiation are essentially inconsequential for PDSI. All other analyses of Pacific Coast surface climate that do not involve PDSI focus on the much higher-quality and more temporally-homogeneous temperature and precipitation data from ClimGrid. Further details and evaluations of these datasets are provided in Williams et al. (2015) (cf. Figure 1, Supplemental Materials therein).

To investigate the robustness of various modes of precipitation variability, we also use version 7 of the Global Precipitation Climatology Centre (GPCC) precipitation dataset (Schneider et al. 2014, 2015). GPCC (available 1901–2013) is a global gridded dataset of monthly precipitation totals interpolated from land surface stations at $1/2^{o}$ spatial resolution. To understand the dynamics underlying precipitation variability and coastal droughts along the Pacific Coast, we use the 200 hPa monthly geopotential height fields from version 2c of the 20^{th} Century Reanalysis (available 1851–2014) (Compo et al. 2011). To analyze possible sea surface temperature (SST) forcing and the influence of ENSO, we use the Hadley Centre SST dataset (1870–present) (HadiSST; Rayner et al. 2003) and the monthly PDO index dataset (1854–present) from the National Centers for Environmental Information at NOAA (https://www.ncdc.noaa.gov/teleconnections/pdo/). We also consider the potential influence of the tropical Atlantic by analyzing the Atlantic Multidecadal Oscillation (AMO) index from the NOAA Earth System Research Laboratory (http://www.esrl.noaa.gov/psd/data/timeseries/AMO/) (Enfield et al. 2001). Finally, we investigate the connection between coastal droughts, precipitation variability, and ARs by analyzing the

AR dataset of Guan and Waliser (2015). This dataset includes information on the location of landfalling ARs calculated from the NCEP-NCAR Reanalysis (1948–2015) at 6-hourly resolution. From this dataset, we compiled a list of the number of AR landfalling days during each cold season (October–March) in each of our Pacific coastal regions (described below).

Analyses

We focus on the CONUS Pacific Coast (126°W–116°W, 32°N–50°N), further subdividing this area into South (126°W–116°W, 32°N–40°N) and North (126°W–116°W, 40°N–50°N) Coast regions. This division along 40°N latitude corresponds with the rough climatological latitude for the storm track and the long-term average boundary between the northern and southern ends of what has been defined as the moisture dipole (Dettinger et al. 1998; Wise 2010, 2016). We apply the following criteria to define widespread drought years during the summer season: 1) PDSI≤ -1 over at least 70% of the entire coastal region (126°W–116°W, 32°N–50°N) and 2) area average PDSI≤ -1 in both the North and South coastal regions. These criteria are designed to identify the most extensive and intensive coastal drought events and position us to evaluate their characteristics and causes. All climate anomalies are calculated relative to a 1921–2000 baseline and the JJA PDSI is recentered to have a zero mean over this same period. All correlations (Spearman's rank) are calculated using linearly detrended data to avoid artificially amplified correlations due to co-occurring, but potentially unrelated, trends.

3. Results and Discussion

a. Precipitation Seasonality and Summer Drought (PDSI)

Most precipitation in the South and North Coast occurs during the cold season from November through April (Figure 1, top panels). North Coast precipitation peaks in November and December,

with a substantial fraction of the seasonal total extending into the early and late spring (April–June). Seasonality is more extreme, and total precipitation lower, in the South Coast, peaking in January and February with very little occurring after April. Point-to-point correlations between monthly precipitation and JJA PDSI highlight the importance of cold season precipitation for summer drought on the CONUS Pacific Coast (Figure 1, bottom panels). Over the North Coast, the strongest correlations with summer PDSI are from November–June, while over the South Coast the largest contribution to summer soil moisture comes from precipitation during December–April.

b. North and South Coast Precipitation and Drought Variability

Since the late 19th century, drought variability (PDSI) between the North and South Coast has been significantly ($p < 0.001$) and positively correlated ($\rho = 0.633$, Figure 2), with apparent in-phase coherence at longer timescales. The latter includes periods of persistent cross-region dryness during the 1920s, 1930s, 1980s, and early 21st century, with anomalous wetness at the turn of the 20th century and in the 1990s. This pan-coastal decadal variability is impressive since it is not a simple result of the PDO, which typically causes opposite sign anomalies in winter precipitation over the North and South Coasts (e.g., McCabe et al. 2004). Further, there is little consistency in PDO state across decades of coherent coastal dryness. For example, the October–March (ONDJFM) PDO was weakly positive during the 1920s (+0.14), more strongly positive during the 1930s (+0.49), but negative during the post-2000 period (–0.35).

This strong covariability is also found in cool season precipitation, which shows similarly significant ($p < 0.001$) positive correlations (Figure 3) between the North and South Coast. The strongest precipitation correlations occur in October–December (OND) and April–May, and are weaker but still significant during January–March (JFM). Precipitation anomalies in both regions may therefore share similar dynamical origins, as indicated by previous studies demonstrating that

high precipitation across the entire Pacific Coast is associated with low pressure and convergence in the region (Cayan and Roads 1984; Klein 1957). This can be seen in the strong negative correlations between North and South Coast precipitation and 200 hPa geopotential heights over the ocean and offshore of the coast (Figure 4), circulation anomalies that would favor enhanced precipitation along the CONUS Pacific Coast. In October-December and January-March the height anomalies resemble internal atmospheric variability, but in April-May there appears a connection to tropical Pacific height anomalies that are likely SST-forced, consistent with the winter to spring intensification of ENSO teleconnections over North America (Jong et al. 2016; McAfee and Wise 2016).

To further clarify contributions of the dipole mode to hydroclimate variability, we conduct a principal component analysis (PCA) on October–March (1902–2013; the overlapping period between the two datasets) precipitation from ClimGrid and GPCC over our restricted Pacific coastal domain and (for GPCC only) a much expanded region of western North America (135°W–112°W, 21°N–60°N). Over the Pacific coastal region (Figure 5, left and center columns), the leading unrotated empirical orthogonal function (EOF) in both ClimGrid and GPCC has a uniform sign across the domain and accounts for $> 40\%$ of the underlying variance. By contrast, the dipole mode, characterized by opposite sign anomalies in the North and South Coast, appears as the second EOF, accounting for $\sim 20\%$ of the total precipitation variance. Only when the analysis domain is expanded over a much broader region (Figure 5, right column) does a quasi dipole-like mode emerge as the leading pattern, with the CONUS west-wide mode as the second EOF, but with neither mode emerging as substantially dominant over the other. Further, the main centers of action in the leading dipole mode in this example are centered in the Pacific Northwest and Southwestern United States, not the North and South Coast regions separated at 40°–42°N.

These results are supported by additional analyses (Figure 6), in which we conduct point-by-

point correlations between October–March precipitation from four cities along the Pacific Coast and GPCC precipitation across western North America. For all four cities, correlations along the CONUS Pacific Coast are mostly same-signed, with a spatial pattern similar to the leading EOF from the restricted coastal EOF analyses. Dipole-like patterns do emerge, but with opposing centers of action in British Columbia and the CONUS Pacific Coast (similar to EOF #2 from the GPCC analysis over the expanded domain). As before, there is little evidence for a dominant dipole pattern along the CONUS Pacific Coast across 40°–42°N.

c. Coastal Droughts

We identified 16 coastal droughts ($\sim$ 13% of years) from 1895–2016 (Figure 7, brown dots in the top panel; individual years listed in the caption). Using a 50% (rather than 70%) drought area threshold resulted in only four more years qualifying as coastal droughts (1928, 1933, 1985, and 1987). Over the entire period of record there is no apparent trend in either occurrence or intensity of these events, though they are unevenly distributed in time, with clusters during persistent periods of co-occurring dryness in the North and South Coast (see Figure 2). The first cluster is during the 1920s and 1930s, a period of some of the worst drought years in California (Mirchi et al. 2013) and the worst multi-year drought in United States history (the Dust Bowl; Schubert et al. 2004). The second major cluster occurred post-2000, coincidentally during a period of persistent La-Niña like conditions in the tropical Pacific likely responsible for drought conditions across much of western North America (Delworth et al. 2015; Seager and Vecchi 2010).

Composite maps of PDSI (median) during coastal drought years confirm that these events are spatially coherent and associated with expansive drought across much of the western CONUS (Figure 7, lower panels). Anomalies in some regions weaken or reverse in the composite for the post-2000 period, when the dominance of cold tropical Pacific forcing shifted the post-2000

baseline climate to more closely reflect a La Niña like pattern. This caused anomalous dryness (Southwest, Texas, and Southeast) and wetness (the Plains and Midwest) that acted to oppose the regional anomalies associated with coastal droughts in the pre-2000 composite, suggesting there is little evidence that La Niña-like states contribute to the clustering of coastal droughts, something we confirm in later analyses.

d. Precipitation and Temperature Anomalies During Coastal Droughts

October through May precipitation anomalies (median calculated across the 16-year drought composite) are negative along the entire Pacific Coast during winters preceding coastal droughts (Figure 8; left column). Area averaged anomalies in the drought composite are 29.2% and 16.8% below normal in the South and North Coast, respectively. There is little consistency, however, in the timing of the most significant prior cool season precipitation deficits during individual drought events (not shown). In 2014, for example, the largest precipitation deficits in both regions occurred relatively early in the cold season (October–January). This contrasts sharply with 1934, when the largest deficits occurred after February.

Anomalous warmth extends across the same region during the droughts (median, calculated across the 16-year drought composite), with the strongest anomalies occurring in maximum temperatures (Figure 8; center and right columns). While anomalous spring–summer warmth in these years can contribute to increasing drought severity through impacts on snow cover and evaporative demand (e.g., Berg and Hall 2017; Williams et al. 2015; Mote et al. 2016), precipitation deficits are the primary driver of historical drought variability in this region (e.g., Seager et al. 2015; Williams et al. 2015). Some of this warmth also likely represents a response to, rather than cause of, these droughts through various mechanisms. These include reduced evaporative cooling from dry soils (Seneviratne et al. 2010), increased surface insolation from lower cloud cover (Wolf et al. 2017;

Yin et al. 2014), or the influence of the blocking ridge in the atmosphere (Singh et al. 2016; Wang et al. 2015).

e. Circulation and Ocean Forcing of Coastal Droughts

The coastal PDSI time series is significantly and negatively correlated with ClimGrid PC #1, the coastal-wide prior winter precipitation mode (Figure 9, left panel). Note that, because of the sign conventions on the PC and EOF, a positive value of PC #1 is associated with negative precipitation anomalies across the CONUS Pacific Coast. Positive values of this mode occur in nearly all coastal droughts (highlighted in brown), consistent with the associated EOF loading and spatially coherent negative precipitation anomalies that characterize these events. The correlation between coastal PDSI and the dipole mode, represented by PC #2, is weak and insignificant (Figure 9, right panel), with coastal droughts occurring during both positive and negative phases of this mode. There are no long-term significant trends in either PC, although PC #1 is biased positive during the drought clusters in the 1920s–1930s and early 21st century (not shown).

PC #1 and the coastal PDSI time series have similar correlation patterns with 200 hPa height anomalies, especially along the west coast of North America (Figure 10, left column). In both cases they reflect the association between wet years and anomalous low pressure off the Pacific Coast and high pressure across the southwest US (similar to Figure 4). These patterns contrast sharply with the precipitation dipole in PC #2, which is associated with negative heights over the midlatitudes and anomalous high pressure in the tropics and over northwestern North America. PC #1 and the coastal PDSI are only weakly correlated with SSTs (Figure 10, right column), with the most significant correlations over the extra-tropical North Pacific and Atlantic. This extra-tropical SST signal in the Pacific most likely reflects the atmosphere forcing the ocean or shifts in the extra-tropical ocean related to tropical Pacific variability (Bond et al. 2015; Davis 1976;

Hartmann 2015), rather than the forcing of the atmosphere by the extra-tropical ocean. However, there is some evidence that such extratropical SST patterns may act as feedbacks to reinforce the coincident atmospheric ridge (Lee et al. 2015; Swain et al. 2016; Wang et al. 2017). Relative to PC #1, however, PC #2 is much more strongly related to ocean variability, including widespread positive correlations with SSTs in the tropical Pacific and Indian Oceans, reflecting the connection to ENSO and PDO variability (e.g., Brown and Comrie 2004; Wise 2010).

The lack of strong correlations between the coastal PDSI time series and either SSTs or the dipole precipitation mode indicates that coastal droughts are most closely linked to internal atmospheric variability, with little to no influence from the ocean. As noted previously, there is little consistency in the seasonal timing of precipitation deficits across droughts, and this dissimilarity extends to the 200 hPa geopotential height and SST anomalies for the extended cold season (October–May) (Figure 11). Coastal droughts occurred during major El Niño (e.g., 1919, 1931, 1966, 1977) and La Niña events (e.g., 1934, 2008), and even in the atmosphere there are a wide diversity of seasonal average circulation patterns that have occurred. Droughts in 1930 and 1934, for example, had strong anomalous ridging centered right along the CONUS west coast, while in other years the high was centered over the ocean (e.g., 2008, 2009) or at higher latitudes over North America (e.g., 1919, 1977).

To quantify the inconsistency in ocean-atmosphere dynamics, we calculated uncentered Spearman's rank pattern correlations between each possible pair of coastal drought years for tropical Pacific SSTs (20°S-20°N, 140°E-70°W, $n = 5600$ grid points) and North Pacific 200 hPa geopotential height anomalies (20°N-70°N, 170°W-100°W, $n = 936$ grid points) for the October–May period. These correlations provide a simple indicator of the level of similarity in the spatial patterns of these anomalies across all events. High positive correlations indicate strong similarity in the spatial pattern of anomalies between two events; strong negative correlations indicate strongly

inverted anomaly fields.

Across all possible pairwise comparisons (Figure 12; 119 for geopotential heights and 120 for SSTs), most correlations are relatively weak ($-0.4 \leq \rho \leq +0.4$; 74 for SSTs, 88 for geopotential heights), indicating a diversity of circulation patterns in the ocean and atmosphere during coastal drought events. A substantial fraction of the correlations are strongly negative ($\rho \leq -0.4$; 23 for SSTs, 15 for geopotential heights). One of the clearest examples of this is 1919, an El Niño year with significant negative height anomalies across the North Pacific, versus 2008, a strong La Niña with positive height anomalies across the mid-latitudes in both hemispheres. We thus find no unified or even dominant set of ocean or atmosphere circulation patterns responsible for coastal droughts, demonstrating that they can arise from a variety of configurations in the ocean–atmosphere system.

For some years, the circulation anomalies in the October–May composites appear contrary to what would be expected during coastal droughts. Droughts in 1919, 1924, 1966, and 1977 (three of them El Niño winters), for example, all show cyclonic circulation anomalies along or near the Pacific Coast that would be expected to increase precipitation on the coast, rather than cause drought. Analyzing atmospheric circulation at a finer seasonal resolution (not shown), however, indicates that all these years have at least one period with anomalous ridging over the west: OND in 1977 and April–May in 1919, 1924, and 1966. These anomaly patterns are concealed in the extended October–May average and consistent with results from the precipitation analysis, demonstrating that summer droughts can arise from precipitation deficits at varying times in the cold season. These findings also further reinforce the importance of internal atmospheric variability for coastal droughts, which is expected to be much more variable from month to month relative to circulation anomalies forced by persistent SSTs.

f. Atmospheric River Analysis

Over the South Coast, PC #1 correlates strongly and significantly ($p \leq 0.001$) with the number of landfalling AR days from October–March (Figure 13, top row), indicating that their frequency in this region is most strongly influenced by the precipitation mode connected to internal atmospheric variability. Correlations with PC #2, by contrast, are weak and insignificant, suggesting little sensitivity to SST-forced storm track shifts. There is also a strong tendency for fewer landfalling ARs over the South Coast during coastal drought events (brown dots in Figure 13). The median number of landfalling AR events in the South Coast in this record (1948–2015) is 23 events per year, compared to a median of 19.5 events across the 10 coastal droughts in this period. This is consistent with previous analyses (Dettinger et al. 2011) that have demonstrated how moisture supplied by a few ARs can "make or break" a drought in this region.

In the North Coast (Figure 13, bottom row), however, the frequency of landfalling ARs is not significantly correlated with PC #1, and there is no clear tendency for fewer landfalling ARs during coastal droughts. In this region, total precipitation is higher and the wet season is longer compared to the South Coast. Total cold season precipitation and subsequent soil moisture availability may therefore be less sensitive to moisture contributions from individual ARs. The frequency of landfalling ARs in the North Coast, however, is significantly ($p \leq 0.001$) correlated with PC #2 and the precipitation dipole. This correlation is much weaker compared to landfalling ARs in the South Coast and PC #1, but suggests some sensitivity of North Coast AR frequency to SST-forced precipitation variability.

4. Conclusions

The dominance of internal atmospheric variability over the SST-forced dipole for hydroclimate along the Pacific Coast has been well understood for years (Cayan and Roads 1984; McGuirk

411 1982), and this perspective holds in our analysis of coastal droughts. Investigating precipitation
412 variability through the lens of the dipole and the associated ENSO/PDO teleconnections is appeal-
413 ing, nevertheless. These dynamics are well characterized and understood, and because of their
414 connection to SSTs there is strong potential for seasonal (and possibly longer) predictability. In-
415 deed, in regions where precipitation and drought variability are dominated by ENSO (e.g., the
416 Southwest US), the dipole and state of ENSO provide important skill for seasonal forecasts. For
417 much of the west, however, and the Pacific Coast in particular, a comprehensive understanding of
418 drought variability and risk requires moving beyond this dipole framework.

419 Widespread coastal drought events occur as a consequence of anomalous ridging near western
420 North America or the Northeast Pacific, deflecting storms and suppressing precipitation along the
421 entire CONUS Pacific Coast. These circulation patterns, and the associated precipitation anoma-
422 lies, arise primarily from internal atmospheric variability, and this is reflected in the lack of con-
423 gruence across events in the seasonal timing of the precipitation deficits and the underlying at-
424 mospheric dynamics. Notably, these droughts are strongly linked to a dearth of landfalling ARs
425 south of 40^{o}N, where they are highly correlated with precipitation PC #1 and internal atmospheric
426 variability. In the North Coast, however, variability in the frequency of landfalling ARs does not
427 contribute substantially to coastal droughts, and shows a modest connection to the SST-forced
428 dipole precipitation mode (PC #2).

429 Despite the clear importance of atmospheric variability, which may be expected to have little
430 interannual or decadal persistence, coastal droughts are not evenly distributed in time, and show
431 some apparent clustering in the 1920s and 1930s and in the early 21st century. These decades
432 corresponded to extended periods of below average moisture availability along the entire Pacific
433 Coast (Figures 2 and 7), suggesting that there may be some source of low-frequency variability
434 modulating drought in this region on decadal timescales. Typically, such memory or persistence

would be expected to originate from decadal ocean dynamics, and the most likely source for this in the western CONUS is the PDO (McCabe et al. 2004). As noted previously, however, there is little consistency in the magnitude or even phasing of the PDO across the main two drought clusters, and it is further well established that PDO teleconnections actually favor out-of-phase moisture anomalies in the meridional direction (McCabe et al. 2004). Warm conditions in the tropical Atlantic (e.g., a positive phase of the AMO) can also act to suppress precipitation across western North America (McCabe et al. 2004; Nigam et al. 2011), with the strongest influence during the fall (Nigam et al. 2011). Positive values of the AMO are associated with positive height anomalies during this season along the entire CONUS Pacific Coast (Figure 3a in Nigam et al. 2011), and so could potentially favor widespread coastal droughts. The AMO during fall (October–December) was positive during the 1930s (+0.164) and post-2000 (+0.192) periods of enhanced coastal dryness, but was near neutral (–0.097) during the arid 1920s. Any connection between Atlantic SSTs and coastal drought variability is therefore highly speculative at this stage. If the apparent clustering of coastal droughts is a robust feature of Pacific Coast hydroclimate, however, there may be potential to constrain the risks of coastal drought occurrence on these decadal and longer timescales, if the source of low frequency variability can be identified.

Our analyses have focused primarily on precipitation variability and the associated dynamics, the main drivers of historical droughts (e.g., Seager et al. 2015). Recent evidence suggests, however, that temperature impacts on evaporative demand and snow are playing an increasingly important role for drought dynamics in the western CONUS (e.g., Berg and Hall 2017; Diffenbaugh et al. 2015; Griffin and Anchukaitis 2014; Mote et al. 2016; Williams et al. 2015). For example, the Pacific Northwest in 2015 (the most recent coastal drought year) experienced a record breaking snow drought, caused by near normal total precipitation but record warmth that resulted in a much diminished snow pack (Fosu et al. 2016; Mote et al. 2016). Snow cover was also exceptionally

low that same year over the Sierra Nevada Mountains due to a combination of high temperatures and low precipitation (Harpold et al. 2017). Warming from climate change is expected to play an increasingly important role in future drought dynamics (e.g., Cook et al. 2015) and the associated impacts, such as wildfire (Abatzoglou and Williams 2016). Accurately assessing the risk and likelihood of coastal droughts in the future may therefore require more explicit consideration of the impact of warming temperatures on relevant processes, and the extent to which this warming may interact with precipitation variability to intensify moisture deficits.

Acknowledgments. BI Cook supported by NASA and the NASA Modeling, Analysis, and Prediction program. JS Mankin was supported in part by an Earth Institute Postdoctoral Fellowship and D Singh was supported by the Lamont-Doherty Postdoctoral Fellowship in Earth and Environmental Science. R Seager, JS Mankin and JE Smerdon were supported in part by NSF grants AGS-1243204 and AGS-1401400. R Seager was additionally supported by NOAA award NA14OAR4310232. AP Williams was supported in part by NSF AGS-1703029 and by the Center for Climate and Life at Columbia University. The AR database is made available by Bin Guan and obtained from https://ucla.box.com/ARcatalog. Lamont contribution #.

References

Abatzoglou, J. T., and A. P. Williams, 2016: Impact of anthropogenic climate change on wildfire across western US forests. *Proceedings of the National Academy of Sciences*, **113 (42)**, 11 770–11 775, doi:10.1073/pnas.1607171113.

Allen, R. G., L. S. Pereira, D. Raes, M. Smith, and Coauthors, 1998: Crop evapotranspiration-Guidelines for computing crop water requirements-FAO Irrigation and drainage, paper 56. *Food and Agriculture Organizatoin of the United Nations, Rome*, **300**, 15pp, URL http://www.fao.org/docrep/x0490e/x0490e07.htm.

Bao, J.-W., S. A. Michelson, P. J. Neiman, F. M. Ralph, and J. M. Wilczak, 2006: Interpretation of Enhanced Integrated Water Vapor Bands Associated with Extratropical Cyclones: Their Formation and Connection to Tropical Moisture. *Monthly Weather Review*, **134 (4)**, 1063–1080, doi:10.1175/MWR3123.1.

Berg, N., and A. Hall, 2017: Anthropogenic warming impacts on California snowpack during drought. *Geophysical Research Letters*, **44 (5)**, 2511–2518, doi:10.1002/2016GL072104.

Bond, N. A., M. F. Cronin, H. Freeland, and N. Mantua, 2015: Causes and impacts of the 2014 warm anomaly in the NE Pacific. *Geophysical Research Letters*, **42 (9)**, 3414–3420, doi:10.1002/2015GL063306.

Brown, D. P., and A. C. Comrie, 2004: A winter precipitation 'dipole' in the western United States associated with multidecadal ENSO variability. *Geophysical Research Letters*, **31 (9)**, n/a–n/a, doi:10.1029/2003GL018726.

Cayan, D. R., M. D. Dettinger, K. T. Redmond, G. J. McCabe, N. Knowles, and D. H. Peterson, 2003: *The Transboundary Setting of California's Water and Hydropower Systems*, 237–262. Springer Netherlands, Dordrecht, doi:10.1007/978-94-015-1250-3{_}11.

Cayan, D. R., and D. H. Peterson, 1989: The influence of North Pacific atmospheric circulation on streamflow in the west. *Aspects of climate variability in the Pacific and the western Americas*, 375–397.

Cayan, D. R., and J. O. Roads, 1984: Local Relationships between United States West Coast Precipitation and Monthly Mean Circulation Parameters. *Monthly Weather Review*, **112 (6)**, 1276–1282, doi:10.1175/1520-0493(1984)112⟨1276:LRBUSW⟩2.0.CO;2.

Coats, S., J. E. Smerdon, B. I. Cook, and R. Seager, 2015: Are Simulated Megadroughts in the North American Southwest Forced? *Journal of Climate*, **28 (1)**, 124–142, doi:10.1175/JCLI-D-14-00071.1.

Cole, J. E., and E. R. Cook, 1998: The changing relationship between enso variability and moisture balance in the continental united states. *Geophysical Research Letters*, **25 (24)**, 4529–4532, doi:10.1029/1998GL900145.

Compo, G. P., and Coauthors, 2011: The Twentieth Century Reanalysis Project. *Quarterly Journal of the Royal Meteorological Society*, **137 (654)**, 1–28, doi:10.1002/qj.776.

Cook, B. I., T. R. Ault, and J. E. Smerdon, 2015: Unprecedented 21st century drought risk in the American Southwest and Central Plains. *Science Advances*, **1 (1)**, doi:10.1126/sciadv.1400082.

Cook, B. I., J. E. Smerdon, R. Seager, and S. Coats, 2014: Global Warming and 21st century drying. *Climate Dynamics*, **43 (9-10)**, 2607–2627, doi:10.1007/s00382-014-2075-y.

Cook, E. R., C. A. Woodhouse, C. M. Eakin, D. M. Meko, and D. W. Stahle, 2004: Long-Term Aridity Changes in the Western United States. *Science*, **306 (5698)**, 1015–1018, doi:10.1126/science.1102586.

Dai, A., 2013: Increasing drought under global warming in observations and models. *Nature Climate Change*, **3 (1)**, 52–58, doi:10.1038/nclimate1633.

Daly, C., M. Halbleib, J. I. Smith, W. P. Gibson, M. K. Doggett, G. H. Taylor, J. Curtis, and P. P. Pasteris, 2008: Physiographically sensitive mapping of climatological temperature and precipitation across the conterminous United States. *International Journal of Climatology*, **28 (15)**, 2031–2064, doi:10.1002/joc.1688.

Daniels, J., 2016: California drought costs to top $600 million. *CNBC*, URL http://www.cnbc.com/2016/08/15/california-drought-costs-to-top-600-million-dollars.html.

Davis, R. E., 1976: Predictability of Sea Surface Temperature and Sea Level Pressure Anomalies over the North Pacific Ocean. *Journal of Physical Oceanography*, **6 (3)**, 249–266, doi:10.1175/1520-0485(1976)006⟨0249:POSSTA⟩2.0.CO;2.

Delworth, T. L., F. Zeng, A. Rosati, G. A. Vecchi, and A. T. Wittenberg, 2015: A Link between the Hiatus in Global Warming and North American Drought. *Journal of Climate*, **28 (9)**, 3834–3845, doi:10.1175/JCLI-D-14-00616.1.

Dettinger, M., 2004: Fifty-two years of "pineapple-express" storms across the West Coast of North America. Tech. rep., US Geological Survey, Scripps Institution of Oceanography for the California Energy Commission.

Dettinger, M. D., 2013: Atmospheric Rivers as Drought Busters on the U.S. West Coast. *Journal of Hydrometeorology*, **14 (6)**, 1721–1732, doi:10.1175/JHM-D-13-02.1.

Dettinger, M. D., D. R. Cayan, H. F. Diaz, and D. M. Meko, 1998: North–South Precipitation Patterns in Western North America on Interannual-to-Decadal Timescales. *Journal of Climate*, **11 (12)**, 3095–3111, doi:10.1175/1520-0442(1998)011⟨3095:NSPPIW⟩2.0.CO;2.

Dettinger, M. D., F. M. Ralph, T. Das, P. J. Neiman, and D. R. Cayan, 2011: Atmospheric rivers, floods and the water resources of california. *Water*, **3 (2)**, 445–478, doi:10.3390/w3020445.

Diaz, H. F., M. P. Hoerling, and J. K. Eischeid, 2001: Enso variability, teleconnections and climate change. *International Journal of Climatology*, **21 (15)**, 1845–1862, doi:10.1002/joc.631.

Dickie, G., 2016: 2015 Wildfires Burned a Record-Breaking 10.1 million acres. *High Country News*, URL http://www.hcn.org/articles/wildfires-burned-a-record-breaking-10-1-million-acres-in-2015.

Diffenbaugh, N. S., D. L. Swain, and D. Touma, 2015: Anthropogenic warming has increased drought risk in California. *Proceedings of the National Academy of Sciences*, **112 (13)**, 3931–3936, doi:10.1073/pnas.1422385112, http://www.pnas.org/content/112/13/3931.full.pdf.

Enfield, D. B., A. M. Mestas-Nuñez, and P. J. Trimble, 2001: The Atlantic Multidecadal Oscillation and its relation to rainfall and river flows in the continental U.S. *Geophysical Research Letters*, **28 (10)**, 2077–2080, doi:10.1029/2000GL012745.

Feng, S., M. Trnka, M. Hayes, and Y. Zhang, 2017: Why Do Different Drought Indices Show Distinct Future Drought Risk Outcomes in the U.S. Great Plains? *Journal of Climate*, **30 (1)**, 265–278, doi:10.1175/JCLI-D-15-0590.1, http://dx.doi.org/10.1175/JCLI-D-15-0590.1.

Fosu, B. O., S.-Y. Simon Wang, and J.-H. Yoon, 2016: The 2014/15 Snowpack Drought in Washington State and its Climate Forcing. *Bulletin of the American Meteorological Society*, **97 (12)**, S19–S24, doi:doi:10.1175/BAMS-D-16-0149.

559 Fuchs, B., 2015: U.S. Drought Monitor, July 7, 2015. National Drought Mitigation Center at
560 the University of Nebraska-Lincoln, URL http://droughtmonitor.unl.edu/data/pngs/20150707/
561 20150707_conus_trd.png.

562 Gimeno, L., R. Nieto, M. VÃzquez, and D. Lavers, 2014: Atmospheric rivers: a mini-review.
563 *Frontiers in Earth Science*, **2**, 2, doi:10.3389/feart.2014.00002.

564 Griffin, D., and K. J. Anchukaitis, 2014: How unusual is the 2012–2014 California drought?
565 *Geophysical Research Letters*, 2014GL062433, doi:10.1002/2014GL062433.

566 Guan, B., and D. E. Waliser, 2015: Detection of atmospheric rivers: Evaluation and application
567 of an algorithm for global studies. *Journal of Geophysical Research: Atmospheres*, **120 (24)**,
568 12 514–12 535, doi:10.1002/2015JD024257.

569 Harpold, A. A., M. Dettinger, and S. Rajagopal, 2017: Defining snow drought and why it matters.
570 *EOS*, **98**, doi:10.1029/2017EO068775.

571 Hartmann, D. L., 2015: Pacific sea surface temperature and the winter of 2014. *Geophysical*
572 *Research Letters*, **42 (6)**, 1894–1902, doi:10.1002/2015GL063083.

573 He, M., M. Russo, and M. Anderson, 2017: Hydroclimatic Characteristics of the 2012–2015
574 California Drought from an Operational Perspective. *Climate*, **5 (1)**, doi:10.3390/cli5010005.

575 Jenkins, D., 2017: WSDA estimates '15 drought damage topped $700 mil-
576 lion. *Capital Press*, URL http://www.capitalpress.com/Washington/20170216/
577 wsda-estimates-15-drought-damage-topped-700-million.

578 Jong, B.-T., M. Ting, and R. Seager, 2016: El Niño's impact on California precipitation: sea-
579 sonality, regionality, and El Niño intensity. *Environmental Research Letters*, **11 (5)**, 054 021,
580 doi:doi:10.1088/1748-9326/11/5/054021.

Kahn, B., 2016: The 2015 Wildfire Season Set an Ominous Record. *Climate Central*, URL http://www.climatecentral.org/news/2015-wildfire-season-sets-ominous-record-19879.

Kintisch, E., 2016: How a "Godzilla" El Niño shook up weather forecasts. *Science*, **352 (6293)**, 1501–1502, doi:10.1126/science.352.6293.1501, http://science.sciencemag.org/content/352/6293/1501.full.pdf.

Klein, W. H., 1957: Principal tracks and mean frequencies of cyclones and anti-cyclones in the Northern Hemisphere. Tech. rep., U.S. Weather Bureau, Washington, DC, 20233. Research Paper No. 40.

Lee, M.-Y., C.-C. Hong, and H.-H. Hsu, 2015: Compounding effects of warm sea surface temperature and reduced sea ice on the extreme circulation over the extratropical North Pacific and North America during the 2013–2014 boreal winter. *Geophysical Research Letters*, **42 (5)**, 1612–1618, doi:10.1002/2014GL062956, 2014GL062956.

Lurie, J., 2015: The Drought Isn't Just a California Problem. *Mother Jones*, URL http://www.motherjones.com/environment/2015/08/drought-isnt-just-california-problem.

Malevich, S. B., and C. A. Woodhouse, 2017: Pacific sea surface temperatures, midlatitude atmospheric circulation, and widespread interannual anomalies in western u.s. streamflow. *Geophysical Research Letters*, **44 (10)**, 5123–5132, doi:10.1002/2017GL073536, URL http://dx.doi.org/10.1002/2017GL073536.

McAfee, S. A., 2014: Consistency and the Lack Thereof in Pacific Decadal Oscillation Impacts on North American Winter Climate. *Journal of Climate*, **27 (19)**, 7410–7431, doi:10.1175/JCLI-D-14-00143.1.

McAfee, S. A., and E. K. Wise, 2016: Intra-seasonal and inter-decadal variability in ENSO impacts on the Pacific Northwest. *International Journal of Climatology*, **36 (1)**, 508–516, doi:10.1002/joc.4351.

McCabe, G. J., and M. D. Dettinger, 2002: Primary Modes and Predictability of Year-to-Year Snowpack Variations in the Western United States from Teleconnections with Pacific Ocean Climate. *Journal of Hydrometeorology*, **3 (1)**, 13–25, doi:10.1175/1525-7541(2002)003⟨0013:PMAPOY⟩2.0.CO;2.

McCabe, G. J., M. A. Palecki, and J. L. Betancourt, 2004: Pacific and Atlantic Ocean influences on multidecadal drought frequency in the United States. *Proceedings of the National Academy of Sciences*, **101 (12)**, 4136–4141, doi:10.1073/pnas.0306738101.

McGuirk, J. P., 1982: A century of precipitation variability along the pacific coast of North America and its impact. *Climatic Change*, **4 (1)**, 41–56, doi:10.1007/BF00143191, URL http://dx.doi.org/10.1007/BF00143191.

Meko, D. M., and C. W. Stockton, 1984: Secular Variations in Streamflow in the Western United States. *Journal of Climate and Applied Meteorology*, **23 (6)**, 889–897, doi:10.1175/1520-0450(1984)023⟨0889:SVISIT⟩2.0.CO;2.

Mirchi, A., K. Madani, M. Roos, and D. W. Watkins, 2013: *Climate Change Impacts on California's Water Resources*, 301–319. Springer Netherlands, Dordrecht, doi:10.1007/978-94-007-6636-5{_}17.

Mitchell, K. E., and Coauthors, 2004: The multi-institution North American Land Data Assimilation System (NLDAS): Utilizing multiple GCIP products and partners in a continen-

tal distributed hydrological modeling system. *Journal of Geophysical Research: Atmospheres*, **109 (D7)**, n/a–n/a, doi:10.1029/2003JD003823.

Monteith, J. L., 1965: Evaporation and Environment. *Symposia of the Society for Experimental Biology*, Vol. 19, 4.

Mote, P. W., and Coauthors, 2016: Perspectives on the causes of exceptionally low 2015 snowpack in the western United States. *Geophysical Research Letters*, n/a–n/a, doi:10.1002/2016GL069965.

Nigam, S., B. Guan, and A. Ruiz-Barradas, 2011: Key role of the Atlantic Multidecadal Oscillation in 20th century drought and wet periods over the Great Plains. *Geophysical Research Letters*, **38 (16)**, doi:10.1029/2011GL048650.

Oyler, J. W., A. Ballantyne, K. Jencso, M. Sweet, and S. W. Running, 2015: Creating a topoclimatic daily air temperature dataset for the conterminous United States using homogenized station data and remotely sensed land skin temperature. *International Journal of Climatology*, **35 (9)**, 2258–2279, doi:10.1002/joc.4127.

Palmer, W. C., 1965: Meteorological drought, Research Paper No. 45. *US Weather Bureau, Washington, DC*, **58**.

Piechota, T. C., and J. A. Dracup, 1996: Drought and Regional Hydrologic Variation in the United States: Associations with the El Niño-Southern Oscillation. *Water Resources Research*, **32 (5)**, 1359–1373, doi:10.1029/96WR00353.

Rayner, N. A., D. E. Parker, E. B. Horton, C. K. Folland, L. V. Alexander, D. P. Rowell, E. C. Kent, and A. Kaplan, 2003: Global analyses of sea surface temperature, sea ice, and night marine air

temperature since the late nineteenth century. *Journal of Geophysical Research*, **108 (D14)**, 4407, doi:10.1029/2002JD002670.

Redmond, K. T., and R. W. Koch, 1991: Surface climate and streamflow variability in the western United States and their relationship to large-scale circulation indices. *Water Resources Research*, **27 (9)**, 2381–2399.

Rice, D., 2015: California drought cost is 2.7 billion in 2015. *USA Today*, URL http://www.usatoday.com/story/weather/2015/08/19/california-drought-cost-27-billion-2015/32007967/.

Rodell, M., and Coauthors, 2004: The Global Land Data Assimilation System. *Bulletin of the American Meteorological Society*, **85 (3)**, 381–394, doi:10.1175/BAMS-85-3-381.

Roman, J., 2015: The Year in Wildfire. *Journal of the National Fire Protection Association*, **November/December**, URL http://www.nfpa.org/newsandpublications/nfpa-journal/2015/november-december-2015/features/the-year-in-wildfire.

Rutz, J. J., W. J. Steenburgh, and F. M. Ralph, 2013: Climatological Characteristics of Atmospheric Rivers and Their Inland Penetration over the Western United States. *Monthly Weather Review*, **142 (2)**, 905–921, doi:10.1175/MWR-D-13-00168.1.

Schneider, U., A. Becker, P. Finger, A. Meyer-Christoffer, B. Rudolf, and M. Ziese, 2015: GPCC Full Data Reanalysis Version 7.0 (at 0.5°, 1.0°, 2.5°): Monthly Land-Surface Precipitation from Rain-Gauges built on GTS-based and Historic Data. doi:10.5676/DWD_GPCC/FD_M_V7_050.

Schneider, U., A. Becker, P. Finger, A. Meyer-Christoffer, M. Ziese, and B. Rudolf, 2014: GPCC's new land surface precipitation climatology based on quality-controlled in situ data and its role in quantifying the global water cycle. *Theoretical and Applied Climatology*, **115 (1-2)**, 15–40, doi:10.1007/s00704-013-0860-x.

Schubert, S. D., M. J. Suarez, P. J. Pegion, R. D. Koster, and J. T. Bacmeister, 2004: On the Cause of the 1930s Dust Bowl. *Science*, **303 (5665)**, 1855–1859, doi:10.1126/science.1095048.

Seager, R., and M. Hoerling, 2014: Atmosphere and Ocean Origins of North American Droughts. *Journal of Climate*, **27 (12)**, 4581–4606, doi:10.1175/JCLI-D-13-00329.1.

Seager, R., M. Hoerling, S. Schubert, H. Wang, B. Lyon, A. Kumar, J. Nakamura, and N. Henderson, 2015: Causes of the 2011 to 2014 california drought. *Journal of Climate*, doi: 10.1175/JCLI-D-14-00860.1.

Seager, R., and G. A. Vecchi, 2010: Greenhouse warming and the 21st century hydroclimate of southwestern North America. *Proceedings of the National Academy of Sciences*, **107 (50)**, 21 277–21 282, doi:10.1073/pnas.0910856107.

Seneviratne, S. I., T. Corti, E. L. Davin, M. Hirschi, E. B. Jaeger, I. Lehner, B. Orlowsky, and A. J. Teuling, 2010: Investigating soil moisture–climate interactions in a changing climate: A review. *Earth-Science Reviews*, **99 (3–4)**, 125 – 161, doi:http://dx.doi.org/10.1016/j.earscirev.2010.02.004.

Sheffield, J., G. Goteti, and E. F. Wood, 2006: Development of a 50-Year High-Resolution Global Dataset of Meteorological Forcings for Land Surface Modeling. *Journal of Climate*, **19 (13)**, 3088–3111, doi:doi:10.1175/JCLI3790.1.

Singh, D., D. L. Swain, J. S. Mankin, D. E. Horton, L. N. Thomas, B. Rajaratnam, and N. S. Diffenbaugh, 2016: Recent amplification of the North American winter temperature dipole. *Journal of Geophysical Research: Atmospheres*, **121 (17)**, 9911–9928, doi:10.1002/2016JD025116.

Swain, D. L., D. E. Horton, D. Singh, and N. S. Diffenbaugh, 2016: Trends in atmospheric patterns conducive to seasonal precipitation and temperature extremes in California. *Science Advances*,

2 (4), doi:10.1126/sciadv.1501344, http://advances.sciencemag.org/content/2/4/e1501344.full.pdf.

Swain, D. L., M. Tsiang, M. Haugen, D. Singh, A. Charland, B. Rajaratnam, and N. S. Diffenbaugh, 2014: The extraordinary California drought of 2013-2014: Character, context, and the role of climate change. *Bulletin of the American Meteorological Society*, **95 (7)**, S3–S7.

Trenberth, K. E., A. Dai, G. van der Schrier, P. D. Jones, J. Barichivich, K. R. Briffa, and J. Sheffield, 2014: Global warming and changes in drought. *Nature Climate Change*, **4 (1)**, 17–22, doi:10.1038/nclimate2067.

Vose, R. S., and Coauthors, 2014: Improved Historical Temperature and Precipitation Time Series for U.S. Climate Divisions. *Journal of Applied Meteorology and Climatology*, **53 (5)**, 1232–1251, doi:10.1175/JAMC-D-13-0248.1.

Wanders, N., and Coauthors, 2017: Forecasting the Hydroclimatic Signature of the 2015/16 El Niño Event on the Western United States. *Journal of Hydrometeorology*, **18 (1)**, 177–186, doi:10.1175/JHM-D-16-0230.1.

Wang, S.-Y. S., W.-R. Huang, and J.-H. Yoon, 2015: The North American winter 'dipole' and extremes activity: a CMIP5 assessment. *Atmospheric Science Letters*, **16 (3)**, 338–345, doi:10.1002/asl2.565.

Wang, S.-Y. S., J.-H. Yoon, R. Gillies, and H.-H. Hsu, 2017: Chapter 13: The California Drought: Trends and Impacts. *Climate Extremes: Patterns and Mechanisms, Geophysical Monograph 226*, 223–234.

Wells, N., S. Goddard, and M. J. Hayes, 2004: A Self-Calibrating Palmer Drought Severity Index. *Journal of Climate*, **17 (12)**, 2335–2351, doi:10.1175/1520-0442(2004)017⟨2335:ASPDSI⟩2.0.CO;2.

Williams, A. P., R. Seager, J. T. Abatzoglou, B. I. Cook, J. E. Smerdon, and E. R. Cook, 2015: Contribution of anthropogenic warming to the 2012–2014 California drought. *Geophysical Research Letters*, **42 (16)**, 6819–6828, doi:10.1002/2015GL064924.

Wise, E. K., 2010: Spatiotemporal variability of the precipitation dipole transition zone in the western United States. *Geophysical Research Letters*, **37 (7)**, n/a–n/a, doi:10.1029/2009GL042193.

Wise, E. K., 2016: Five centuries of U.S. West Coast drought: Occurrence, spatial distribution, and associated atmospheric circulation patterns. *Geophysical Research Letters*, **43 (9)**, 4539–4546, doi:10.1002/2016GL068487.

Wolf, S., D. Yin, and M. L. Roderick, 2017: Using radiative signatures to diagnose the cause of warming during the 2013â2014 Californian Drought. *Journal of Hydrology*, –, doi:https://doi.org/10.1016/j.jhydrol.2017.07.015.

Woodhouse, C. A., J. L. Russell, and E. R. Cook, 2009: Two Modes of North American Drought from Instrumental and Paleoclimatic Data. *Journal of Climate*, **22 (16)**, 4336–4347, doi:10.1175/2009JCLI2705.1.

Yin, D., M. L. Roderick, G. Leech, F. Sun, and Y. Huang, 2014: The contribution of reduction in evaporative cooling to higher surface air temperatures during drought. *Geophysical Research Letters*, **41 (22)**, 7891–7897, doi:10.1002/2014GL062039.

LIST OF FIGURES

Fig. 1. In the top panels, long-term (1896–2016) mean (top left) and fraction of Water–Year total (top right) precipitation for October through September precipitation over the South (126°W–116°W, 32°N–40°N) and North (126°W–116°W, 40°N–50°N) Coast (black dashed boxes). Bottom panels show correlations between summer average (June-July-August; JJA) self-calibrating Palmer Drought Severity Index (PDSI) and antecedent or concurrent monthly precipitation in the ClimGrid dataset. October through December precipitation fields are taken from the preceding year of the JJA PDSI. 37

Fig. 2. Regional average summer (June-July-August; JJA) self-calibrating Palmer Drought Severity Index (PDSI) from the North and South Coast for 1895–2016 (top left). PDSI variability between the two regions is strongly and significantly positively correlated ($\rho = 0.633$, $p \leq 0.001$; right), indicating a tendency for in-phase summer moisture anomalies across the two regions. The October–March (ONDJFM) average PDO index is also shown, highlighting the lack of coherence between PDO phasing and coastal drought variability. 38

Fig. 3. Regional average precipitation (mm/day) comparisons between the North and South Coast regions for the fall and early winter (October-November-December, OND; left panel), winter and early spring (January-February-March, JFM; center panel), and spring (April-May; right panel). Black dashed lines indicate the mean precipitation for each region and season, calculated from our baseline period (1921-2000). 39

Fig. 4. Correlations between average precipitation for the South and North Coast and 200 hPa geopotential height anomalies for different seasonal windows: October-November-December, January-February-March, and April-May. Areas of negative correlation (blue) indicate low pressure anomalies associated with high precipitation in the South or North Coast. Insignificant correlations ($p > 0.10$) are masked by the grey dots. 40

Fig. 5. The two leading unrotated empirical orthogonal functions (EOFs) from a principal component analysis of cold season (October-March; ONDJFM) precipitation in the ClimGrid and Global Precipitation Climatology Centre (GPCC) datasets from 1902–2013 (the overlapping period between ClimGrid and GPCC). In the first two columns, the analysis domain is restricted to the combined North and South Coast region. In the right column, the domain is expanded over a much larger region of western North America (135°W–112°W, 21°N–60°N). Inset numbers indicate the percent of total ONDJFM precipitation variance represented by each mode. 41

Fig. 6. Point-by-point correlations between GPCC cold season (October-March; ONDJFM) precipitation and precipitation from four west coast cities: Juneau, Alaska; Seattle, Washington; San Francisco, California; Los Angeles, California. City precipitation was generated by averaging precipitation in all grid cells within 1° latitude and longitude of the approximate city locations (red dots). 42

Fig. 7. Area averaged PDSI (top panel) for the combined North and South Coast. Dashed lines indicate average or normal conditions (zero mean for the 1921-2000 baseline). The 16 coastal drought events identified in our study are marked by the brown dots: 1919, 1924, 1929, 1930, 1931, 1934, 1966, 1977, 1994, 2002, 2004, 2007, 2008, 2009, 2014, 2015. In the lower panels, composite summer PDSI (median) for all coastal drought years ($n = 16$), coastal drought years before 2000 ($n = 9$), coastal drought years after 2000 ($n = 7$), and PDSI for 2000–2016 ($n = 17$). 43

Fig. 8. Composite (median) precipitation (% of normal) and maximum and minimum temperature (K) anomalies in the ClimGrid dataset during the 16 coastal drought years for fall and early winter (OND), winter and early spring (JFM), April-May, and summer (JJA). All anomalies are calculated relative to the average from the 105 non-drought years. 44

Fig. 9. Comparisons (1896–2016) between the coastal average PDSI and PC #1 and PC #2 from the EOF analysis of October–March ClimGrid precipitation. For this, and subsequent analyses, the EOF analysis was expanded from 2013 through 2016 in order to capture all the coastal droughts. Spearman's rank correlation are shown in the upper right corners and coastal drought years are indicated by the brown dots. 45

Fig. 10. Point-by-point correlations (Spearman's rank) for the ClimGrid PCs and coastal PDSI versus October–March 200 hPa geopotential heights from the 20th Century Reanalysis (1896–2014) (left column) and HadiSST sea surface temperatures (1896–2016) (right column). Insignificant correlations ($\rho > 0.10$) are masked by the grey dots. 46

Fig. 11. For each coastal drought event, October–May average anomalies in 200 hPa geopotential height (contours, meters) and sea surface temperatures (shading, K). Because the 20th Century Reanalysis ends in 2014, height anomalies for the 2015 event were not available. . . . 47

Fig. 12. Pairwise uncentered pattern correlations between October–May anomalies in sea surface temperatures (lower left panels) and 200 hPa geopotential heights (upper right panels) for all coastal drought years. Strong positive correlations indicate similar spatial patterns in either geopotential height anomalies (e.g., 1931 versus 1977) or sea surface temperatures (e.g., 1919 versus 1931) between two coastal drought years. The spatial domains used to calculate the pattern correlations are shown in the bottom panel. 48

Fig. 13. Correlations between atmospheric river landfalling days (October–March) in the South and North Coast regions and the ClimGrid precipitation PCs. The atmospheric river record extends from 1948–2015; coastal droughts occurring during this period (1966, 1977, 1994, 2002, 2004, 2007, 2008, 2009, 2014, 2015) are highlighted in brown. 49

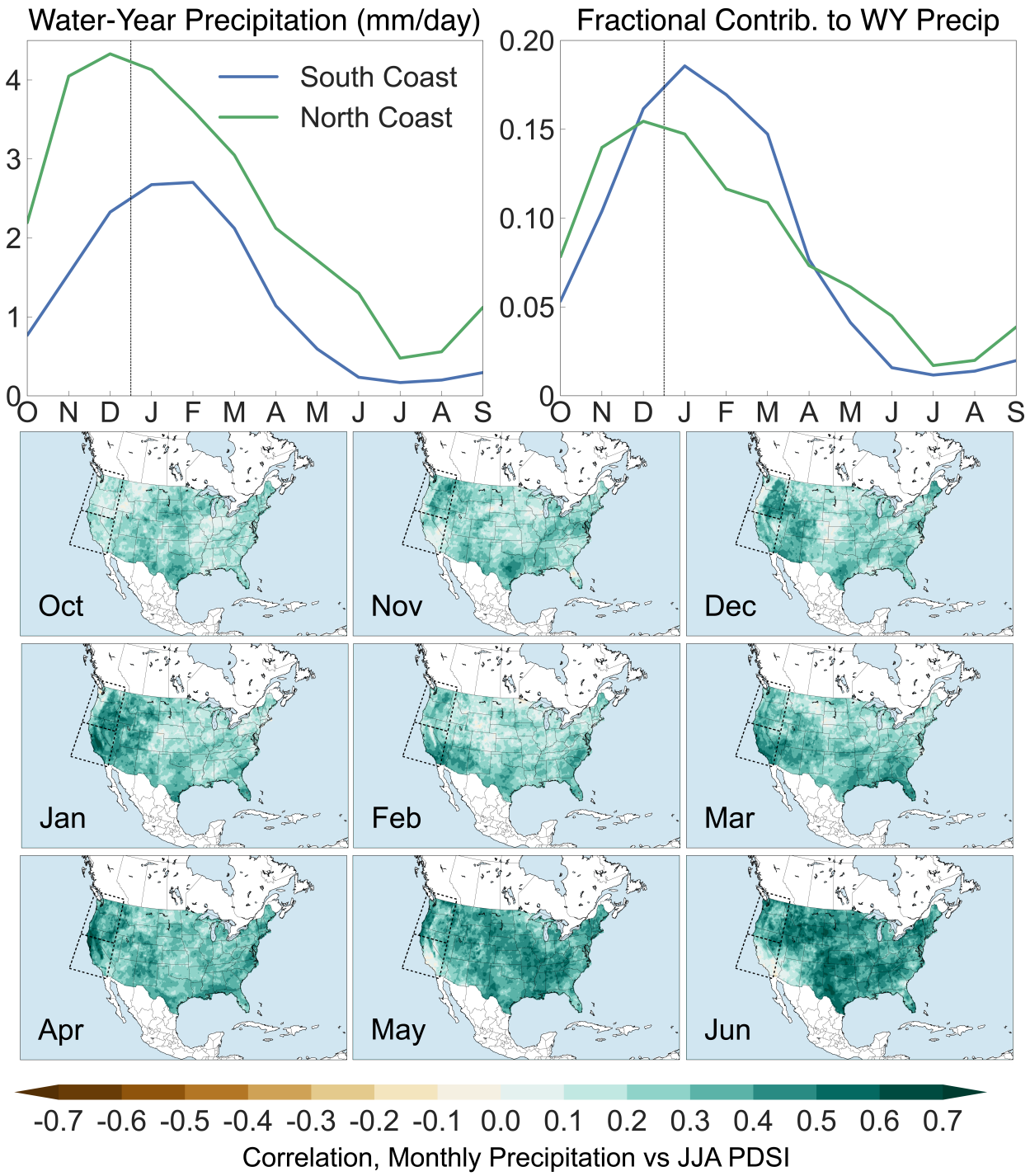

FIG. 1. In the top panels, long-term (1896–2016) mean (top left) and fraction of Water–Year total (top right) precipitation for October through September precipitation over the South (126°W–116°W, 32°N–40°N) and North (126°W–116°W, 40°N–50°N) Coast (black dashed boxes). Bottom panels show correlations between summer average (June-July-August; JJA) self-calibrating Palmer Drought Severity Index (PDSI) and antecedent or concurrent monthly precipitation in the ClimGrid dataset. October through December precipitation fields are taken from the preceding year of the JJA PDSI.

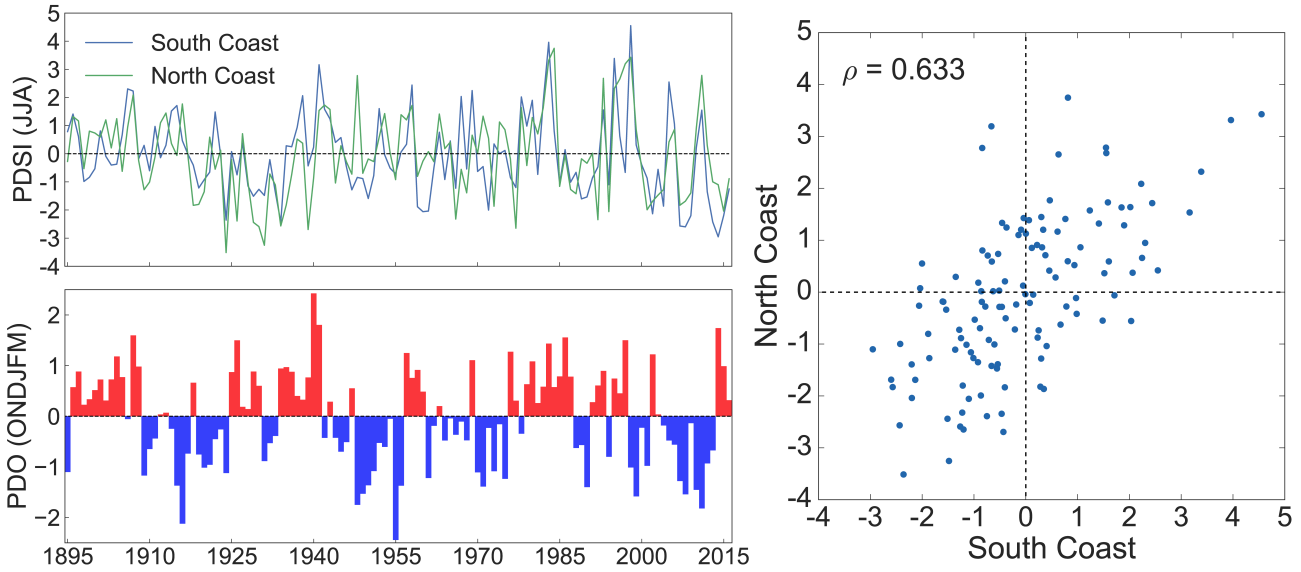

805 FIG. 2. Regional average summer (June-July-August; JJA) self-calibrating Palmer Drought Severity Index
806 (PDSI) from the North and South Coast for 1895–2016 (top left). PDSI variability between the two regions is
807 strongly and significantly positively correlated ($\rho = 0.633$, $p \leq 0.001$; right), indicating a tendency for in-phase
808 summer moisture anomalies across the two regions. The October–March (ONDJFM) average PDO index is also
809 shown, highlighting the lack of coherence between PDO phasing and coastal drought variability.

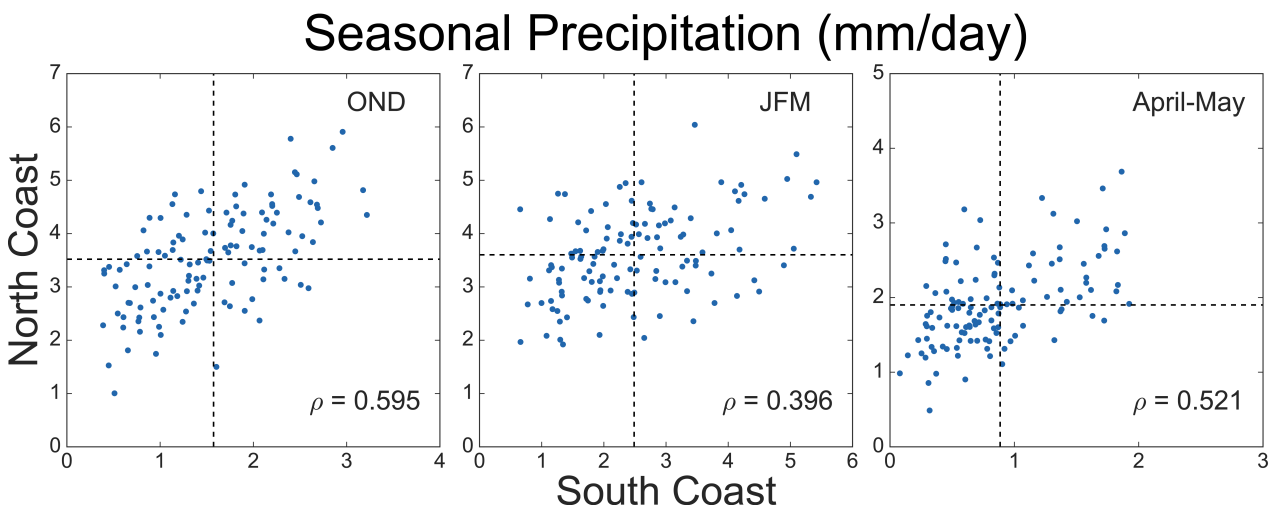

FIG. 3. Regional average precipitation (mm/day) comparisons between the North and South Coast regions for the fall and early winter (October-November-December, OND; left panel), winter and early spring (January-February-March, JFM; center panel), and spring (April-May; right panel). Black dashed lines indicate the mean precipitation for each region and season, calculated from our baseline period (1921-2000).

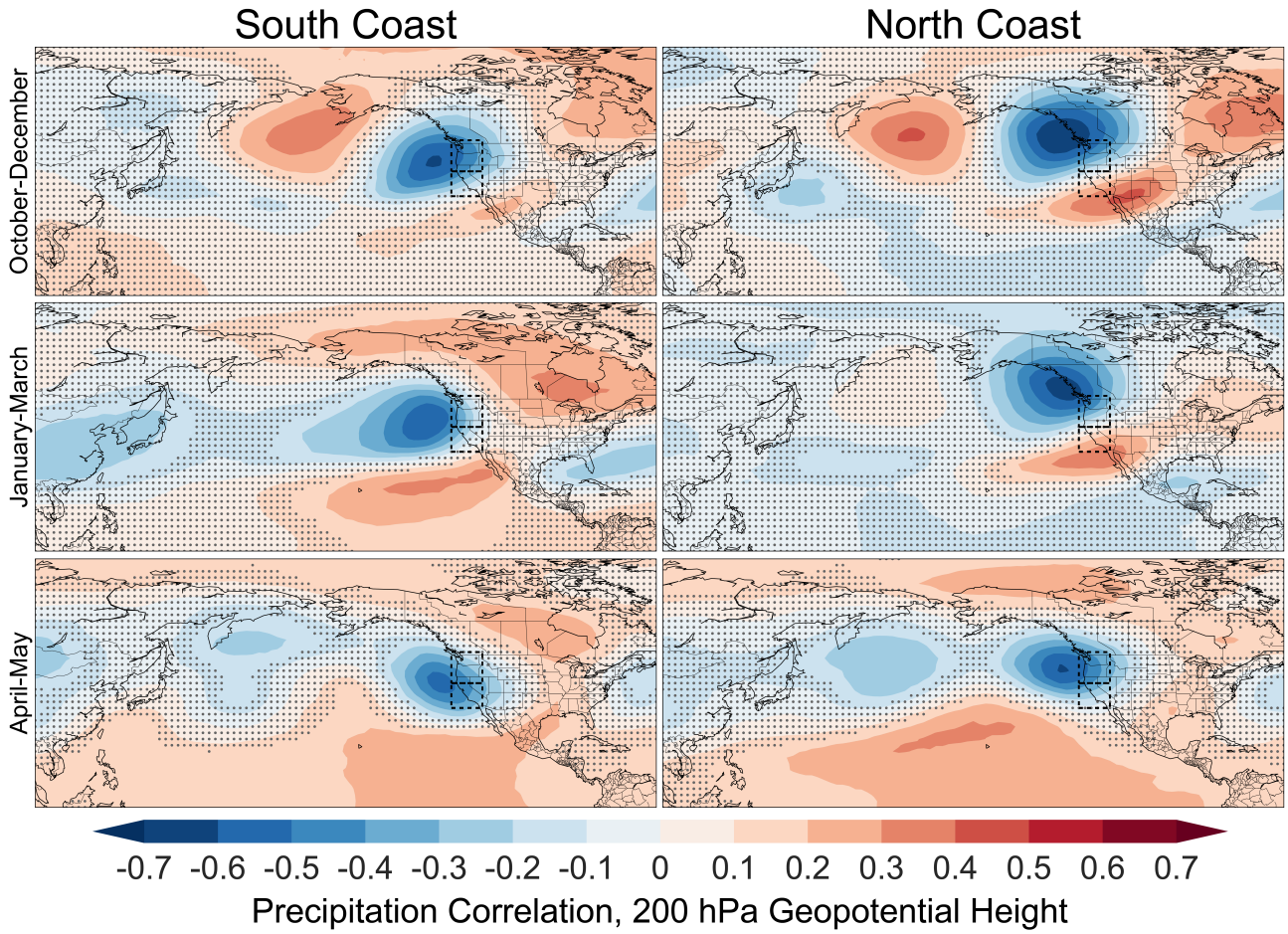

FIG. 4. Correlations between average precipitation for the South and North Coast and 200 hPa geopotential height anomalies for different seasonal windows: October-November-December, January-February-March, and April-May. Areas of negative correlation (blue) indicate low pressure anomalies associated with high precipitation in the South or North Coast. Insignificant correlations ($p > 0.10$) are masked by the grey dots.

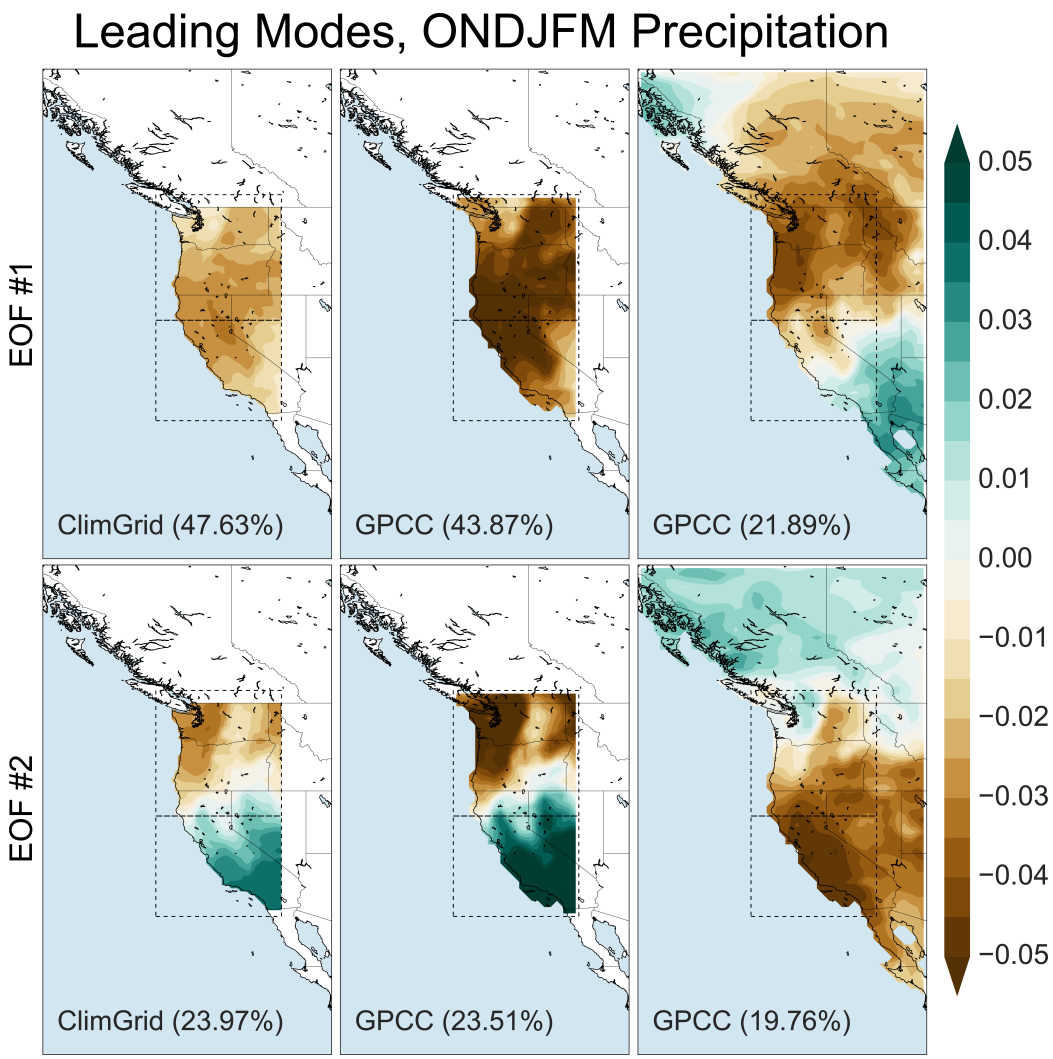

FIG. 5. The two leading unrotated empirical orthogonal functions (EOFs) from a principal component analysis of cold season (October-March; ONDJFM) precipitation in the ClimGrid and Global Precipitation Climatology Centre (GPCC) datasets from 1902–2013 (the overlapping period between ClimGrid and GPCC). In the first two columns, the analysis domain is restricted to the combined North and South Coast region. In the right column, the domain is expanded over a much larger region of western North America (135°W–112°W, 21°N–60°N). Inset numbers indicate the percent of total ONDJFM precipitation variance represented by each mode.

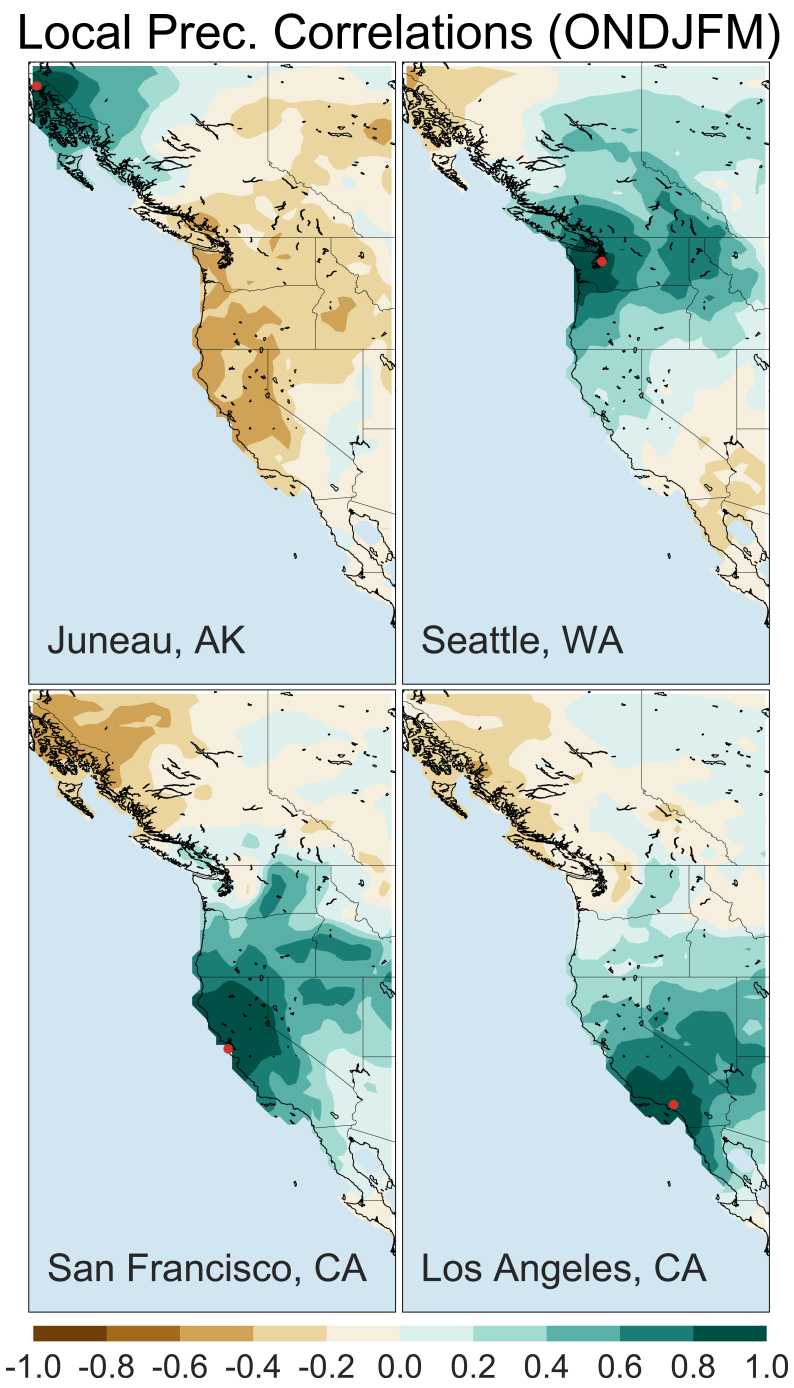

824 FIG. 6. Point-by-point correlations between GPCC cold season (October-March; ONDJFM) precipitation
825 and precipitation from four west coast cities: Juneau, Alaska; Seattle, Washington; San Francisco, California;
826 Los Angeles, California. City precipitation was generated by averaging precipitation in all grid cells within 1°
827 latitude and longitude of the approximate city locations (red dots).

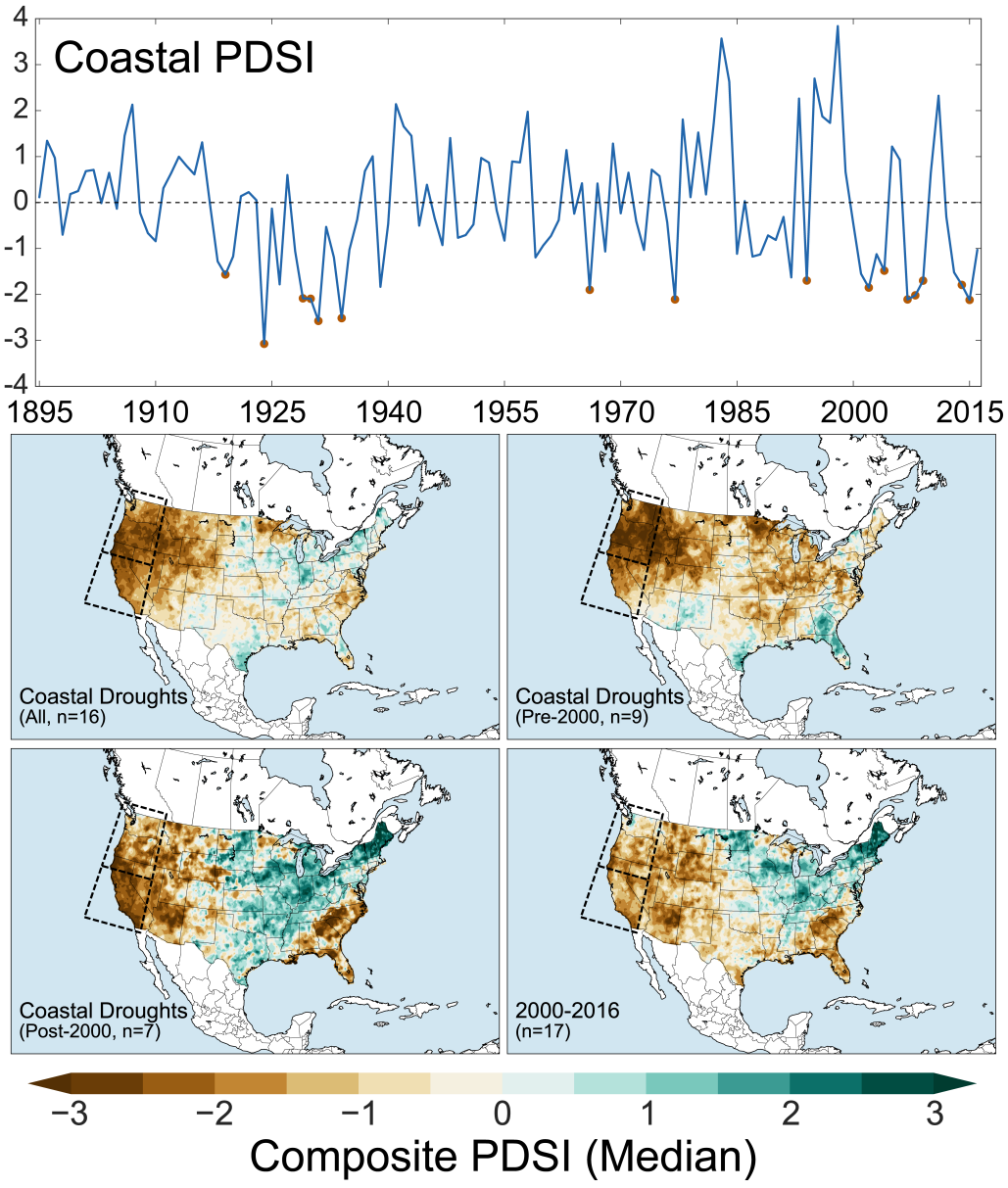

828 FIG. 7. Area averaged PDSI (top panel) for the combined North and South Coast. Dashed lines indicate
829 average or normal conditions (zero mean for the 1921-2000 baseline). The 16 coastal drought events identified
830 in our study are marked by the brown dots: 1919, 1924, 1929, 1930, 1931, 1934, 1966, 1977, 1994, 2002, 2004,
831 2007, 2008, 2009, 2014, 2015. In the lower panels, composite summer PDSI (median) for all coastal drought
832 years ($n = 16$), coastal drought years before 2000 ($n = 9$), coastal drought years after 2000 ($n = 7$), and PDSI
833 for 2000–2016 ($n = 17$).

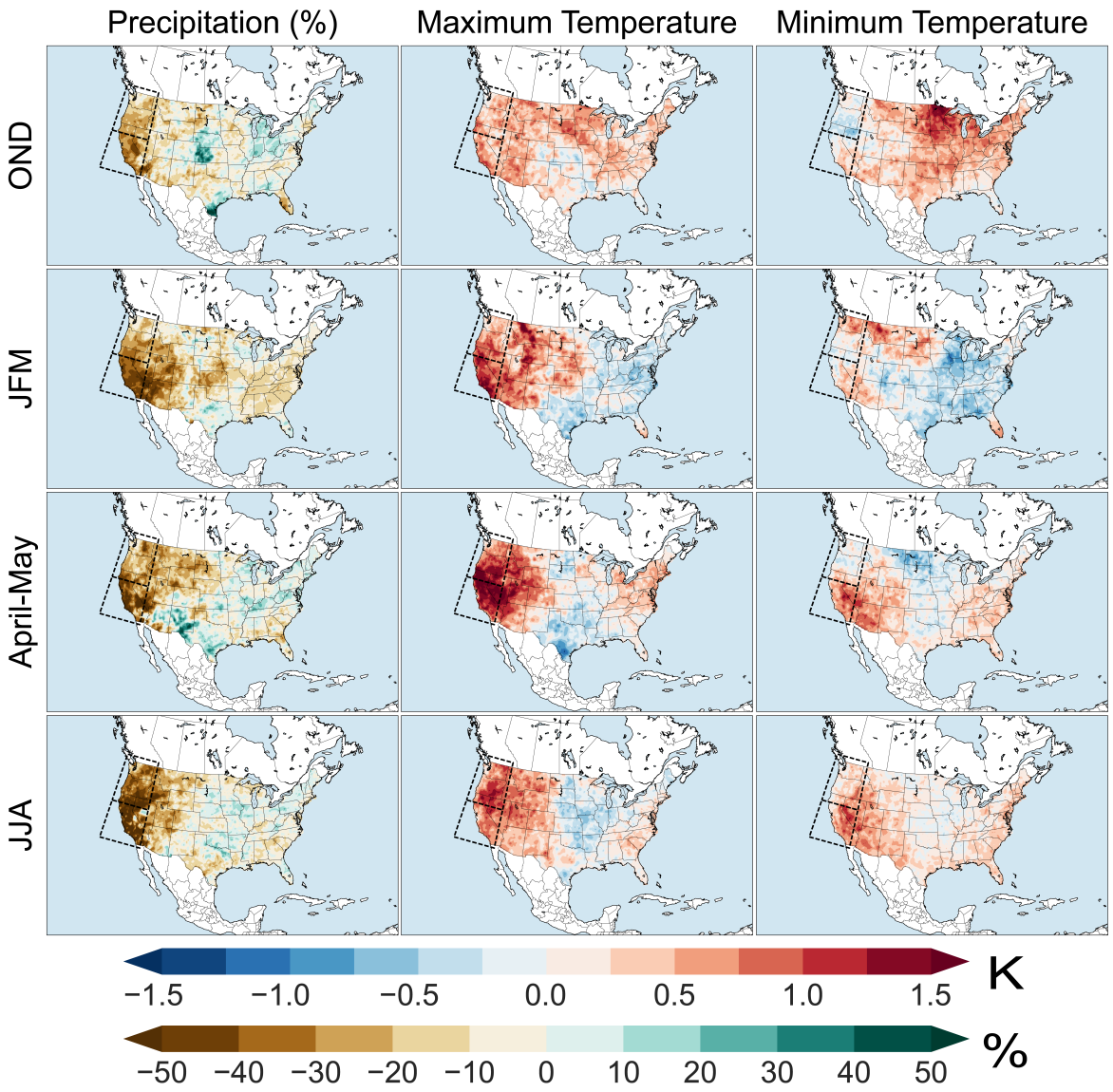

834 FIG. 8. Composite (median) precipitation (% of normal) and maximum and minimum temperature (K) anoma-
835 lies in the ClimGrid dataset during the 16 coastal drought years for fall and early winter (OND), winter and early
836 spring (JFM), April-May, and summer (JJA). All anomalies are calculated relative to the average from the 105
837 non-drought years.

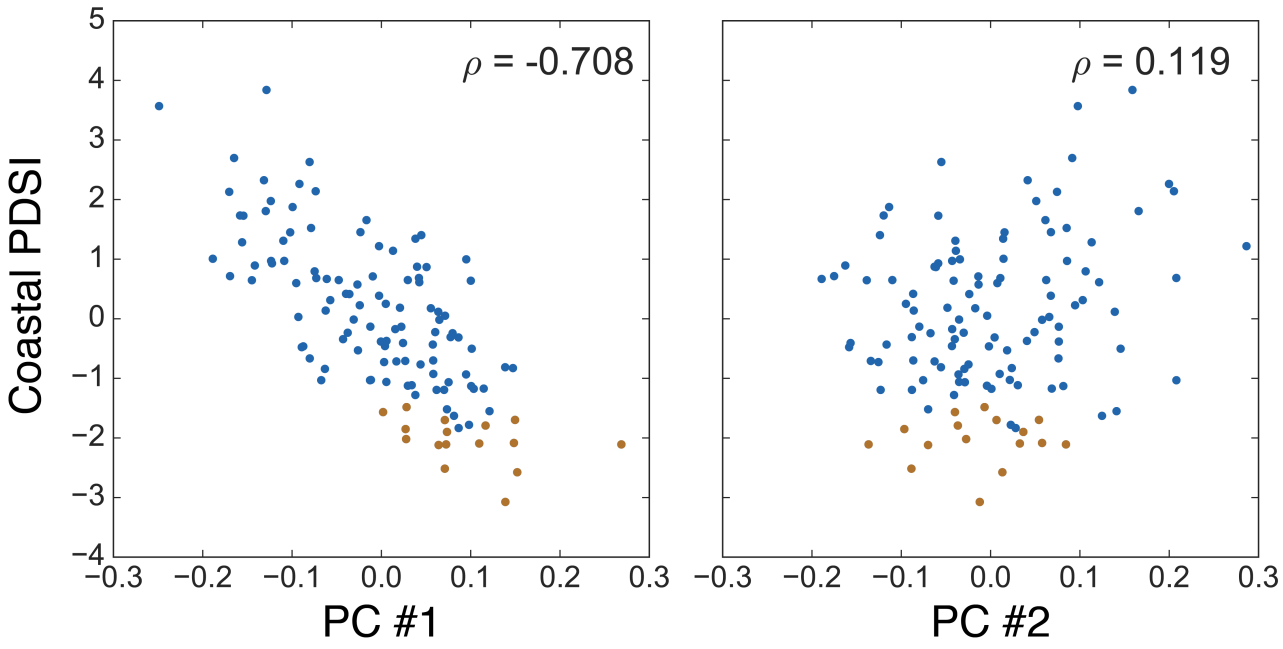

838 FIG. 9. Comparisons (1896–2016) between the coastal average PDSI and PC #1 and PC #2 from the EOF
839 analysis of October–March ClimGrid precipitation. For this, and subsequent analyses, the EOF analysis was
840 expanded from 2013 through 2016 in order to capture all the coastal droughts. Spearman's rank correlation are
841 shown in the upper right corners and coastal drought years are indicated by the brown dots.

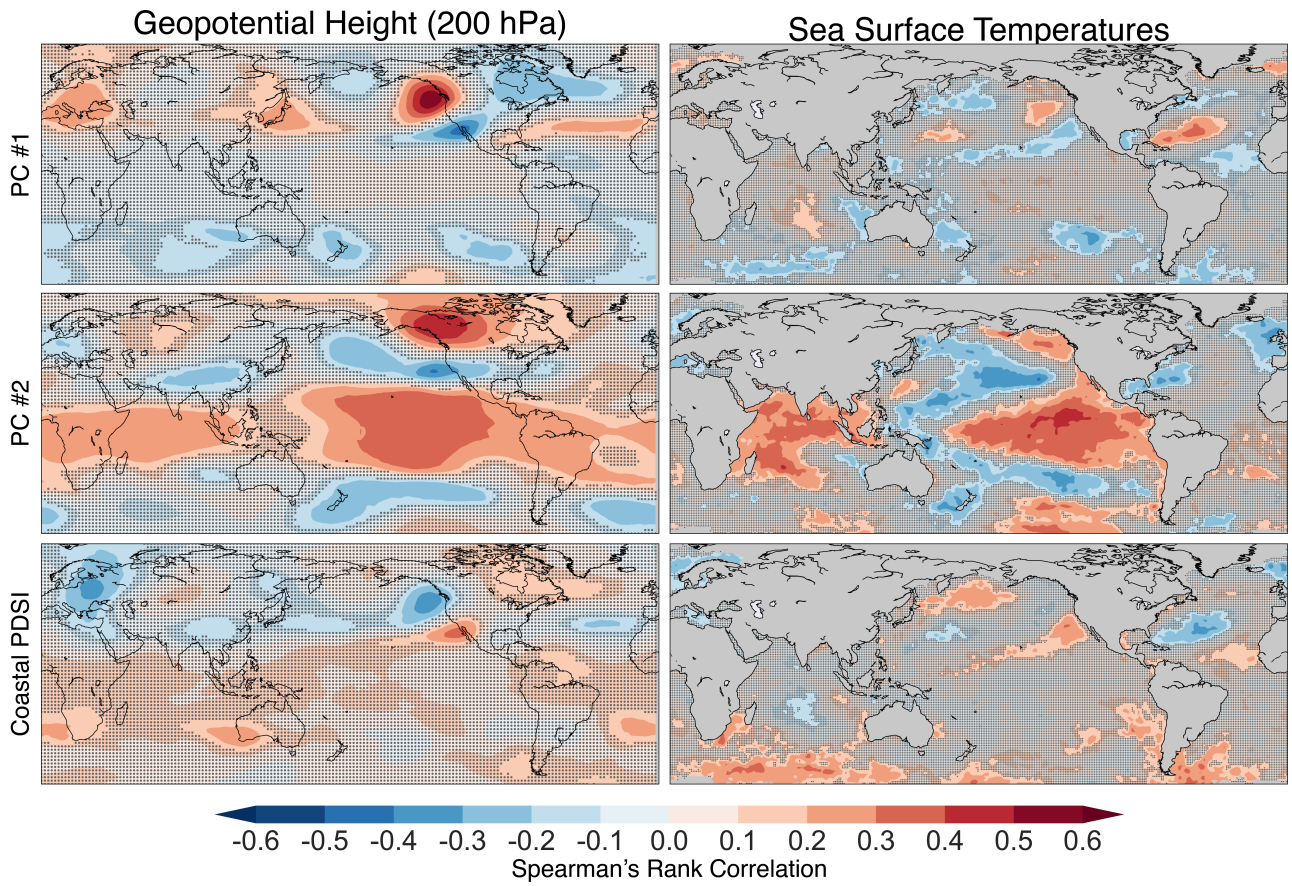

FIG. 10. Point-by-point correlations (Spearman's rank) for the ClimGrid PCs and coastal PDSI versus October–March 200 hPa geopotential heights from the 20th Century Reanalysis (1896–2014) (left column) and HadiSST sea surface temperatures (1896–2016) (right column). Insignificant correlations ($\rho > 0.10$) are masked by the grey dots.

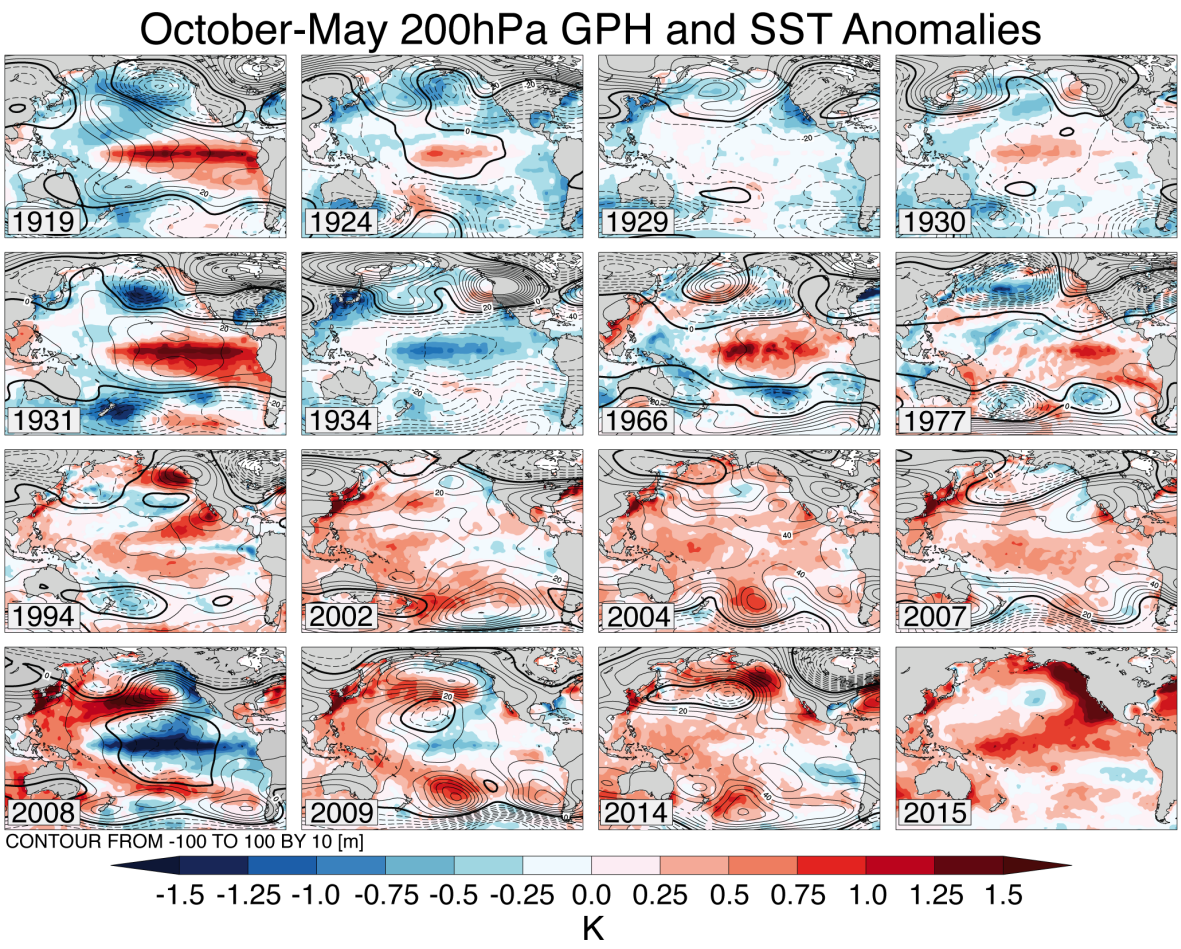

FIG. 11. For each coastal drought event, October–May average anomalies in 200 hPa geopotential height (contours, meters) and sea surface temperatures (shading, K). Because the 20th Century Reanalysis ends in 2014, height anomalies for the 2015 event were not available.

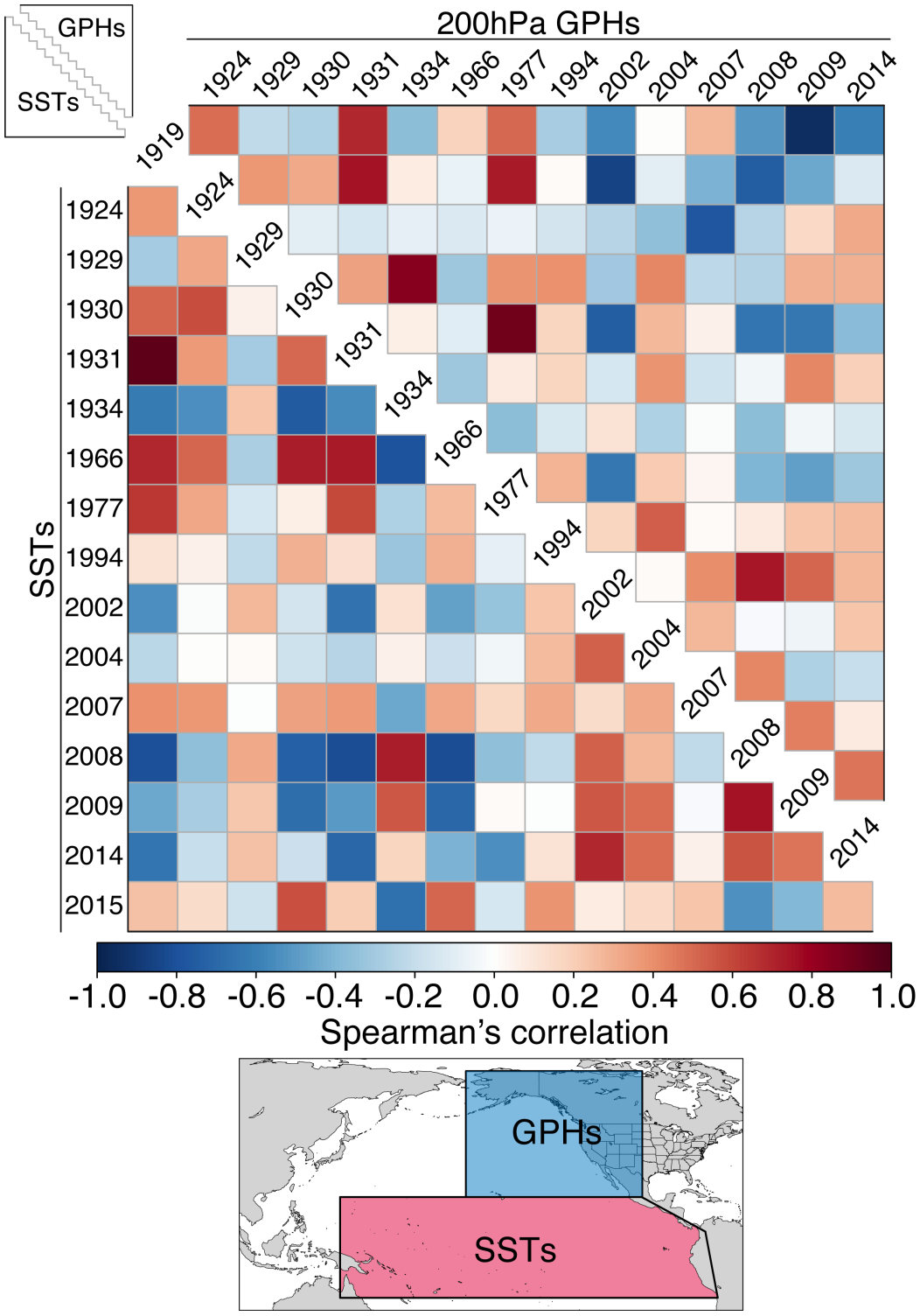

849 FIG. 12. Pairwise uncentered pattern correlations between October–May anomalies in sea surface temper-
850 atures (lower left panels) and 200 hPa geopotential heights (upper right panels) for all coastal drought years.
851 Strong positive correlations indicate similar spatial patterns in either geopotential height anomalies (e.g., 1931
852 versus 1977) or sea surface temperatures (e.g., 1919 versus 1931) between two coastal drought years. The spatial
853 domains used to calculate the pattern correlations are shown in the bottom panel.

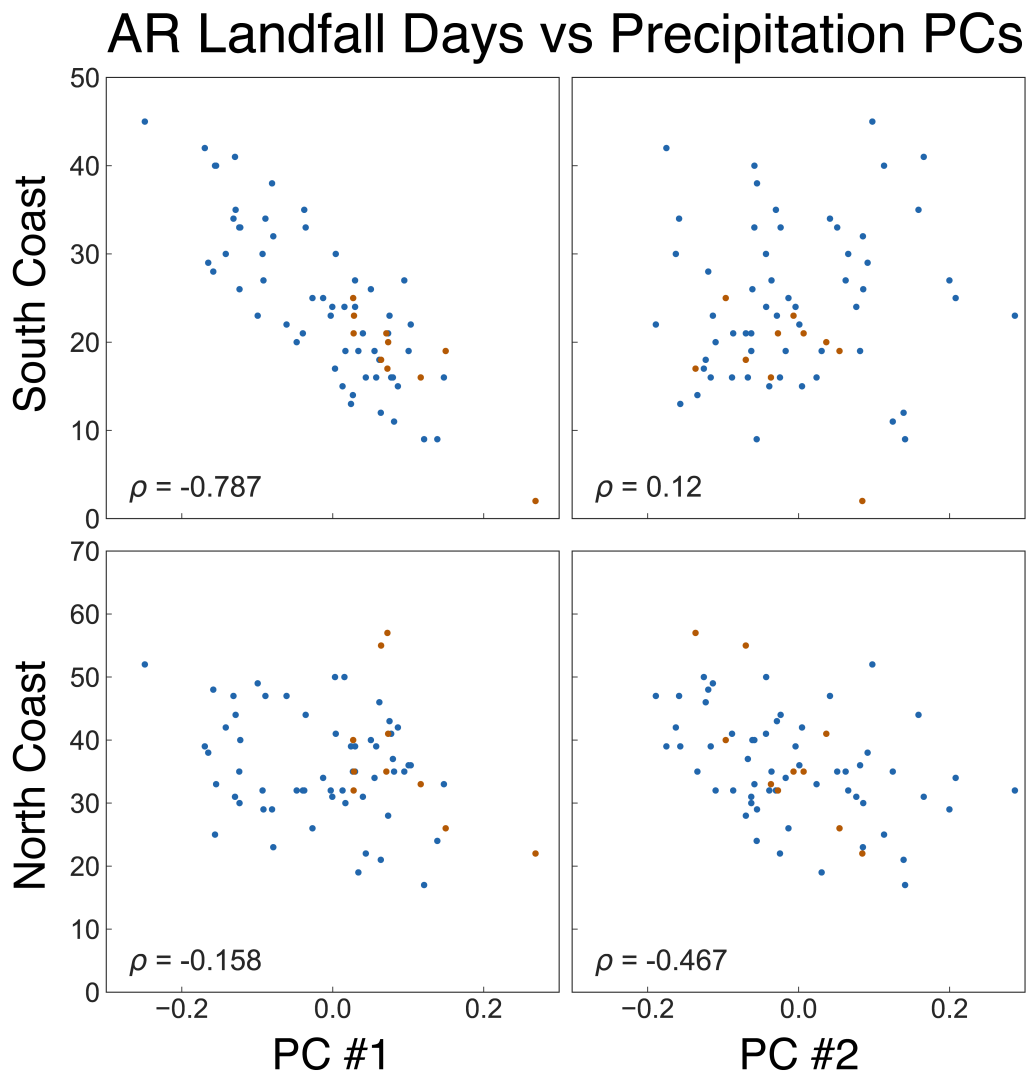

FIG. 13. Correlations between atmospheric river landfalling days (October–March) in the South and North Coast regions and the ClimGrid precipitation PCs. The atmospheric river record extends from 1948–2015; coastal droughts occurring during this period (1966, 1977, 1994, 2002, 2004, 2007, 2008, 2009, 2014, 2015) are highlighted in brown.